Research Square

Preprints are preliminary reports that have not undergone peer review.
They should not be considered conclusive, used to inform clinical practice,
or referenced by the media as validated information.

Apigenin is a direct small-molecule inhibitor of LAG-3 that synergizes with PD-L1 blockade for cancer immunotherapy

Konrad Barnowski
Jagiellonian University
Marzena Lenart
Jagiellonian University
Ping Lv
Zhejiang University of Technology
Sylwia Wojcik
Jagiellonian University
Katarzyna Nakielska
Jagiellonian University
Justyna Kocik-Krol
Jagiellonian University
Judyta Cielecka-Piontek
Poznan University of Medical Sciences
Anna Stasiłowicz-Krzemień
Poznan University of Medical Sciences
Fusco Riccardo
Palacký University Olomouc
Alexander Doemling
Palacký University Olomouc
Justyna Kalinowska-Tłuścik
Jagiellonian University
Marta Karpiel
Jagiellonian University
Szymon Buda
Jagiellonian University
Katarzyna Magiera-Mularz
Jagiellonian University
Ewa Surmiak
Jagiellonian University
Bogdan Musielak

Jagiellonian University

Maciej Siedlar
Jagiellonian University

Bozena Skupien-Rabian
Jagiellonian University

Urszula Jankowska
Jagiellonian University

Wen Zhang
Zhejiang University of Technology

Jacek Plewka
jacek.plewka@uj.edu.pl

Jagiellonian University

Research Article

Keywords:

Posted Date: August 18th, 2026

DOI: https://doi.org/10.21203/rs.3.rs-10713654/v1

License: This work is licensed under a Creative Commons Attribution 4.0 International License.
Read Full License

Additional Declarations: No competing interests reported.

Apigenin is a direct small-molecule inhibitor of LAG-3 that synergizes with PD-L1 blockade for cancer immunotherapy

Konrad Barnowski [a,b], Marzena Lenart [c], Ping Lv [d], Sylwia Wójcik [a,b], Katarzyna Nakielska [a,c], Justyna Kocik-Król [a], Judyta Cielecka-Piontek[g], Anna Stasiłowicz-Krzemień[g], Fusco Riccardo [e], Alexander Doemling [e], Justyna Kalinowska-Tłuścik [a], Marta Karpiel [a,b], Szymon Buda [a], Katarzyna Magiera-Mularz [a], Ewa Surmiak [a], Bogdan Musielak [a], Maciej Siedlar [c], Bozena Skupien-Rabian [f,h], Urszula Jankowska [f,h], Wen Zhang* [d], Jacek Plewka* [a]

[a]Faculty of Chemistry, Jagiellonian University, Gronostajowa 2, 30-387 Krakow, Poland;

[b]Jagiellonian University, Doctoral School of Exact and Natural Sciences, prof. St. Łojasiewicza 11, 30-348 Krakow, Poland

[c]Department of Clinical Immunology, Institute of Pediatrics, Jagiellonian University Medical College, Wielicka 265, 30-663 Krakow, Poland

[d]Lab of Chemical Biology and Molecular Drug Design, College of Pharmaceutical Science, Zhejiang University of Technology, Deqing 313299, China

[e]Czech Advanced Technology and Research Institute (CATRIN), Palacký University Olomouc, Šlechtitelů 27, 77900 Olomouc, Czech Republic

[f] Proteomics Core Facility, Malopolska Centre of Biotechnology, Jagiellonian University, Krakow, Poland

[g]Department of Pharmacognosy and Biomaterials, Poznan University of Medical Sciences, Rokietnicka 3, 60-806 Poznan, Poland

[h]Proteomics Core Facility, Faculty of Biochemistry, Biophysics and Biotechnology, Jagiellonian University, Krakow, Poland

*Email: jacek.plewka@uj.edu.pl wzhang63@zjut.edu.cn

Abstract

Background

Immune checkpoint blockade targeting PD-1/PD-L1 and LAG-3 has demonstrated significant clinical benefit. The recent FDA approval of combined LAG-3 and PD-1 blockade (relatlimab plus nivolumab) shows the clinical value of dual checkpoint inhibition. Current strategies rely almost exclusively on monoclonal antibodies, and the development of small-molecule modulators of LAG-3 remains largely unexplored. Here, we investigate whether apigenin, a naturally occurring flavonoid with reported anticancer and immunomodulatory properties, can serve as a small-molecule alternative to anti-LAG-3 antibodies in combination immunotherapy.

Methods

Flavonoids were screened for disruption of the LAG-3/MHCII interaction using HTRF. Binding of apigenin was validated by molecular dynamics, microscale thermophoresis and chemoproteomic pull-down. Functional activity and combination

effects with the anti-PD-L1 antibody durvalumab were assessed in Jurkat reporter assays and human PBMCs, with synergy quantified using Bliss independence modeling. A polymeric formulation was developed to improve solubility and reduce nonspecific cytotoxicity. Antitumor efficacy was evaluated in a syngeneic MC38 mice model expressing human PD-L1.

Results

Apigenin disrupted the LAG-3/MHCII interaction and directly bound LAG-3 in cells, without detectable activity against PD-1/PD-L1. Functionally, formulated apigenin restored T-cell activation and worked synergistically with durvalumab, yielding uniformly positive Bliss-independence scores (peaking at ΔBliss ≈ 0.20) within a non-toxic concentration range enabled by formulation. In primary human PBMCs, the combination increased CD69 and CD137 expression and raised IFN-γ production. Quantitative proteomics showed a coordinated reprogramming of T-cell programs, with up-regulation of immune-activation and leukocyte-migration pathways and down-regulation of extracellular-matrix and tissue-remodeling programs associated with immune exclusion. In vivo, combination therapy significantly improved tumor growth inhibition, increased the intratumoral $CD8^+$T-cell frequency, and raised granzyme B and perforin expression without detectable toxicity.

Conclusions

Apigenin is a direct small-molecule inhibitor of LAG-3 that disrupts the LAG-3/MHCII interface and synergizes with PD-L1 blockade to increase antitumor immunity. These findings show that an inhibitory immune receptor traditionally addressed only by biologics can be engaged by a small molecule, and support antibody–small-molecule combinations as a strategy for dual checkpoint immunotherapy.

Introduction

Immune checkpoint blockade has transformed the treatment of many cancers, producing durable responses across multiple malignancies [1]. Antibodies targeting the PD-1/PD-L1 axis in particular have demonstrated broad clinical efficacy. However, a substantial fraction of patients either fail to respond or relapse after an initial response, reflecting both intrinsic and adaptive mechanisms of immune resistance [2]. This has motivated combinatorial strategies designed to counteract the compensatory inhibitory pathways that limit single-agent checkpoint blockade. Among these, lymphocyte-activation gene 3 (LAG-3), an inhibitory receptor expressed on activated and exhausted T cells [3], is one of the most clinically advanced targets. The approval of the relatlimab–nivolumab combination for advanced melanoma established LAG-3 as the third clinically validated checkpoint and confirmed that PD-1 and LAG-3 exert non-redundant control over T-cell dysfunction [4].

LAG-3 is a transmembrane protein structurally related to CD4 that binds major histocompatibility complex class II (MHCII) molecules, negatively regulating T-cell activation and proliferation [5,6]. In addition to MHCII, fibrinogen-like protein 1 (FGL1) has been identified as an alternative ligand that mediates immunosuppression within the tumor microenvironment independently of antigen presentation [7], and the LAG-3/FGL1 axis has since been linked to immune-evasive tumor phenotypes and clinical outcomes [8]. LAG-3 is frequently co-expressed with PD-1 on chronically stimulated or exhausted T cells within inflamed tumor microenvironments [9,10]. Mechanistically, the two receptors act through separate routes: PD-1 attenuates proximal T-cell receptor signaling through recruitment of the phosphatase SHP2 [11], while LAG-3 sustains functional exhaustion and impairs effector responses. This complementary regulation provides the biological rationale for dual blockade: co-inhibition of PD-1 and LAG-3 produces synergistic antitumor effects in preclinical models and in the clinic.

Despite this strong rationale, therapeutic targeting of LAG-3 remains confined to monoclonal antibodies and related biologics. While effective, antibodies carry well-recognized limitations, including high manufacturing cost, restricted tumor and tissue penetration, and the need for parenteral administration. Small-molecule immune modulators offer other advantages, including oral bioavailability, tunable pharmacokinetics, and lower production complexity, and have begun to reach the PD-1/PD-L1 field [12,13]. The LAG-3/MHCII contact, however, is a large and shallow protein–protein interface, the archetypal "undruggable" target class for which small-molecule antagonists are notoriously difficult to develop. To date, no well-characterized small-molecule inhibitor of LAG-3 has been successfully tested on mice, leaving a gap between the biological validation of the target and the chemical means to drug it.

Flavonoids are a structurally diverse class of dietary polyphenols that modulate the tumor microenvironment and have repeatedly been shown to potentiate immune-checkpoint blockade, making them an attractive scaffold for the systematic discovery of checkpoint-directed small molecules [14,15]. Apigenin (4′,5,7-trihydroxyflavone), a flavone abundant in many fruits and vegetables, is among the best studied, with well-documented antioxidant, anti-inflammatory, and anticancer activities, exerted in part through modulation of the PI3K/Akt, NF-κB, and STAT signaling pathways and induction of apoptosis [16]. In the immune compartment specifically, apigenin has been reported to increase T-cell–mediated tumor killing, an effect attributed to STAT1-dependent transcriptional suppression of PD-L1 in tumor and dendritic cells [17,18]. Every immunomodulatory activity described for apigenin to date, however, has been interpreted as an indirect consequence of altered signaling or gene expression. Whether apigenin engages any immune-checkpoint protein directly has never been examined.

Interpretation of apigenin's biology is further complicated by its poor aqueous solubility and high crystallinity, which promote nonspecific cytotoxicity at the elevated concentrations often used in vitro [19,20]. Many prior studies employed non-formulated apigenin, making it difficult to separate genuine immunomodulatory mechanisms from

stress- and aggregation-related artifacts, a confound that is especially acute for a polyphenol, a chemical class prone to nonspecific, PAINS-like behaviour. Amorphous solid-dispersion formulation offers a well-established route to improve solubility and suppress these artifacts [21], and is therefore a prerequisite for defining apigenin's true, concentration-controlled activity.

In this study, we identify apigenin as a direct small-molecule inhibitor of LAG-3 and show that it disrupts the LAG-3/MHCII interaction without detectable activity against the PD-1/PD-L1 interaction, a binding-level preference that is mechanistically distinct from apigenin's previously described effects on PD-L1 expression. Using a structure–activity screen of 36 flavonoids, orthogonal biophysical binding assays, and photoaffinity-labeling chemoproteomics that identifies LAG-3 as the dominant cellular target, we establish direct engagement in a native cellular context. We also develop a polymeric formulation that eliminates nonspecific cytotoxicity and reveals apigenin's checkpoint-specific activity within a physiologically relevant, low-micromolar range, and we quantify its cooperation with the anti-PD-L1 antibody durvalumab in reporter and primary human T-cell assays. Finally, we show that co-administration of formulated apigenin with durvalumab increases antitumor efficacy and promotes cytotoxic T-cell responses in a PD-L1-humanized MC38 mice model. These findings establish apigenin as a direct small-molecule inhibitor of LAG-3 and provide proof of concept for dual checkpoint inhibition using an antibody–small-molecule combination.

Results

A flavone structure–activity relationship identifies apigenin as a potent LAG-3/MHCII disruptor

Flavonoids show potential as adjuvants in cancer immunotherapy because they can modulate the tumor microenvironment and increase the efficacy of immune checkpoint blockade [14]. To identify small-molecule modulators of the LAG-3 immune checkpoint, we screened a panel of 36 structurally diverse flavonoids, spanning flavones, flavonols, flavanones, flavanonols, and isoflavones, for their ability to disrupt the LAG-3/MHCII interaction using a homogeneous time-resolved fluorescence (HTRF) assay. Nine compounds exhibited measurable inhibitory activity, with IC_{50} values spanning the low-to-mid micromolar range (14–248 μM; Table 1, Figure 1C), while the remaining 27 were inactive ($IC_{50} \gg 300$ μM).

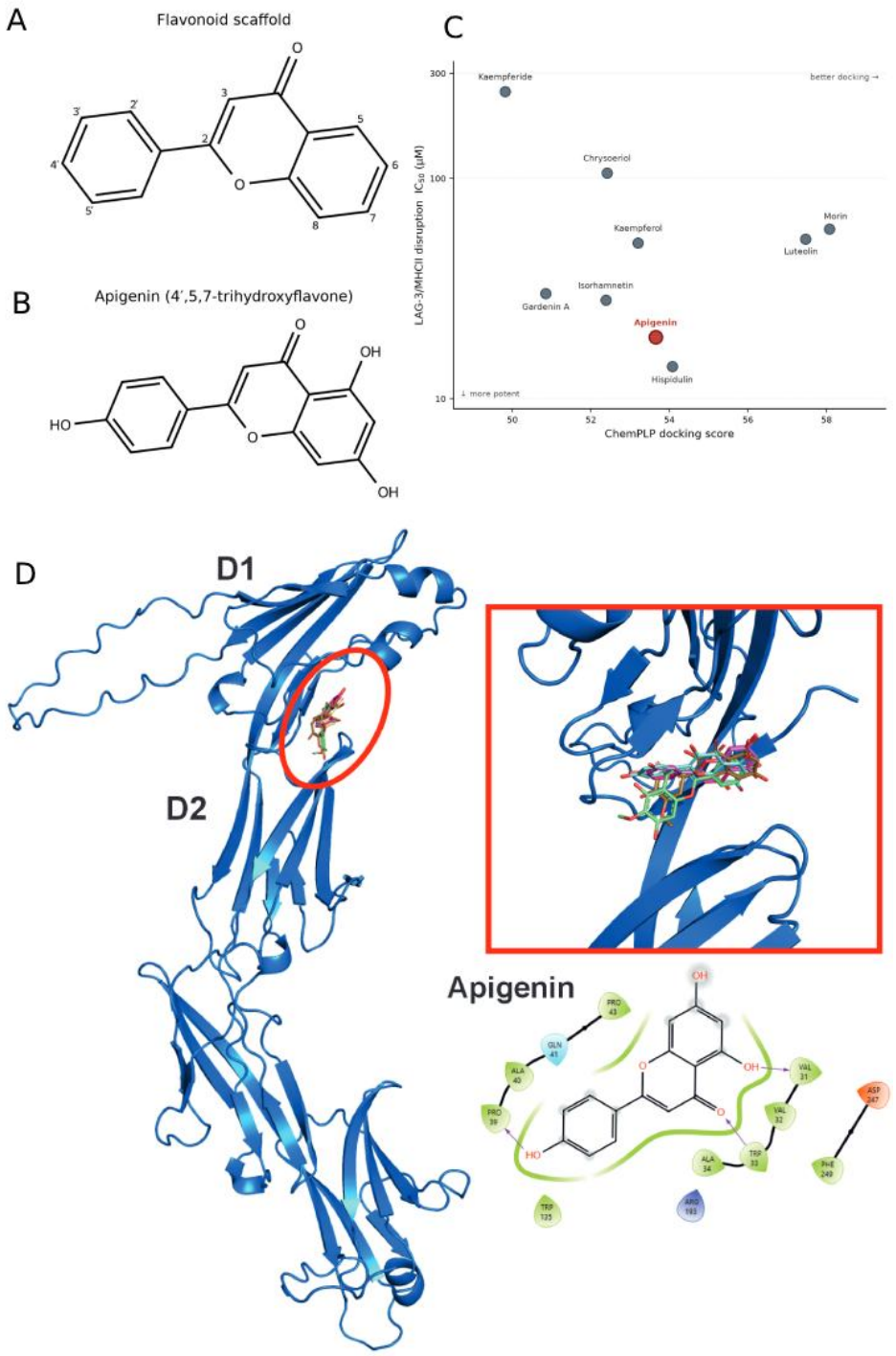
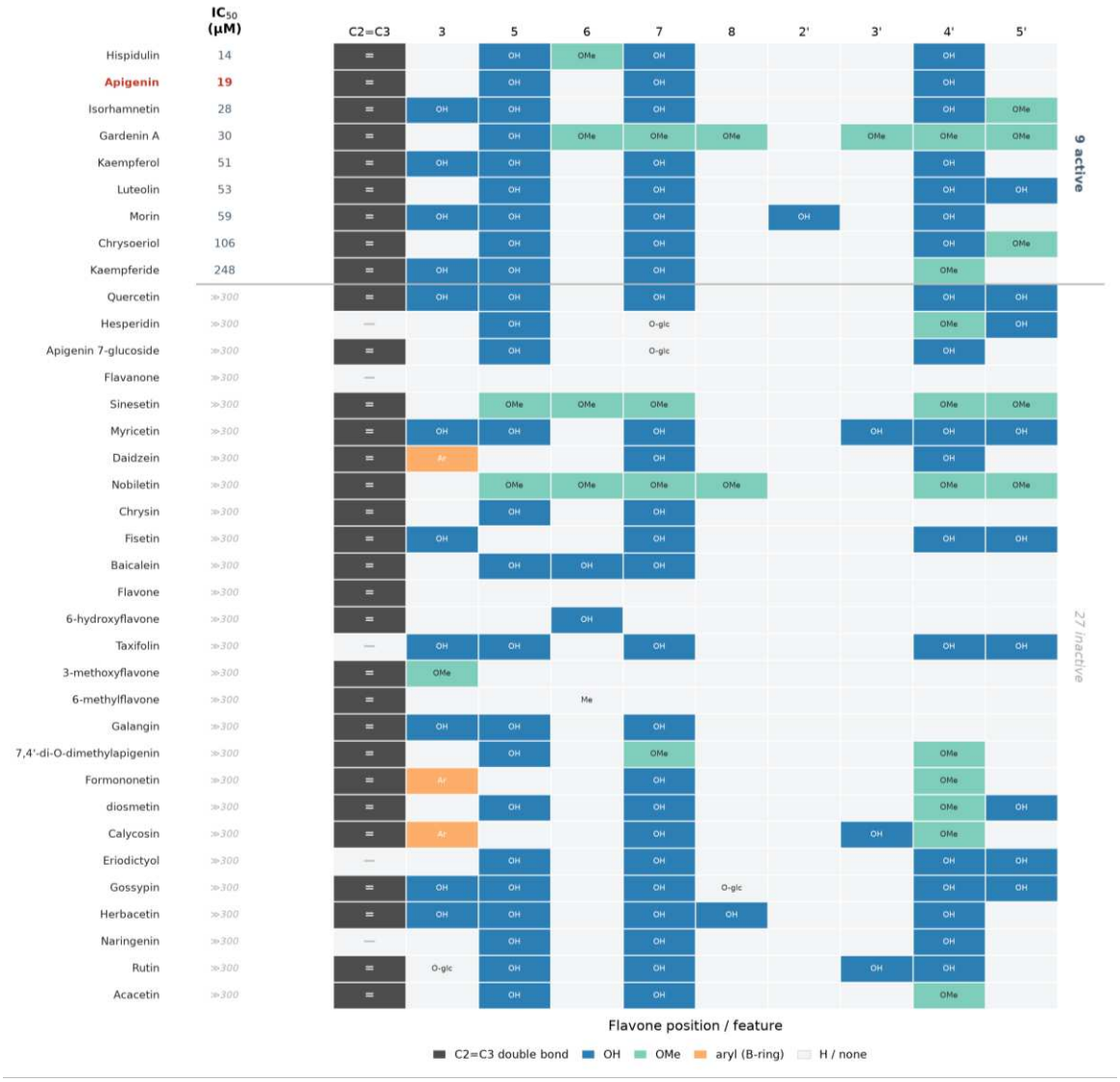


Figure 1. Flavonoid structure–activity relationship for disruption of the LAG-3/MHCII interaction. (A) Flavonoid scaffold with the A, B, and C rings and IUPAC ring positions labeled. (B) Structure of apigenin (4′,5,7-trihydroxyflavone), one of the most potent disruptor identified. (C) ChemPLP docking score plotted against LAG-3/MHCII disruption IC_{50} (log scale) for the nine active compounds; apigenin is highlighted in red. (D) Predicted binding mode of apigenin in human LAG-3 (model based on the 9BF9 template) from molecular docking and MD simulation, shown with the receptor cartoon, the docked-ligand overlay of the five most potent flavonoids, and the two-dimensional protein–ligand interaction map for apigenin; key contact residues include Trp33, Val31/Val32, Ala34, the Pro39–Pro43 loop, Phe249, and Asp247.

Table 1. Structure–activity relationship (SAR) results for LAG-3/MHCII disruption in HTRF screening. The table summarizes 36 flavonoids tested for their ability to dissociate the LAG-3/MHCII complex. Position in the table correspond to the general motif



Rather than segregating by flavonoid subclass, activity tracked a defined structural pharmacophore (Figure 1A). Two features were strictly required: a C2–C3 double bond and a free 5-hydroxyl group, both present in every active compound. Naringenin illustrates the importance of this feature: although it shares the identical 5,7,4′-trihydroxy substitution pattern with apigenin, it is a flavanone lacking the C2–C3 double bond and showed no detectable activity. Free hydroxyls at positions 7 and 4′ were strongly favorable, present in 89% and 78% of active compounds respectively, whereas 3′-hydroxylation and glycosylation at any position abolished activity. Within this active pharmacophore, potency was further tuned by peripheral substitution: a 3-hydroxyl group, the feature distinguishing flavonols from flavones, was tolerated but consistently lowered potency (mean IC_{50} ≈ 96 μM for 3-hydroxylated compounds versus ≈ 44 μM without), and methylation of the 4′-hydroxyl was similarly detrimental, as seen for kaempferide (IC_{50} 248 μM). Methoxylation at position 6, in contrast, was well tolerated and compatible with high potency, exemplified by hispidulin (6-OMe), the most potent compound in the screen (IC_{50} 14 μM). The most potent hits included hispidulin, apigenin (Figure 1B), isorhamnetin, kaempferol, and luteolin, all of which have previously been associated with anticancer activity [16,22–25]. These

observations define a compact structural rule, a planar flavone core bearing free 5-, 7-, and 4′-hydroxyls, that governs LAG-3/MHCII modulation.

None of the active flavonoids disrupted the interaction between LAG-3 and its alternative ligand FGL1, despite the partial overlap of their binding surfaces within the LAG-3 D1 domain (Figure S1A). This finding suggests that flavonoid-mediated inhibition is preferential for the LAG-3/MHCII interface rather than reflecting nonspecific interference with LAG-3 ligand recognition. To further assess checkpoint selectivity, representative compounds were evaluated in an orthogonal PD-1/PD-L1 HTRF assay. Neither apigenin nor structurally related flavonoids showed measurable activity against the PD-1/PD-L1 interaction (Figure S1B). NMR binding experiments likewise failed to detect direct interaction between apigenin and PD-L1, despite the presence of motifs similar to biphenyl which are found in several reported PD-L1 inhibitors [26–29] (Figure S1C). These results show that flavonoid-mediated inhibition is not a general property across immune checkpoint interfaces, and argue against nonspecific aggregation-driven or PAINS-like mechanisms frequently associated with polyphenolic compounds. To validate direct target engagement, we employed microscale thermophoresis (MST) as an orthogonal biophysical assay. Apigenin bound recombinant LAG-3 with an affinity of approximately 15 μM (Figure S1D), in good agreement with its activity in the HTRF assay. These data establish apigenin as a direct small-molecule inhibitor of LAG-3, with LAG-3/MHCII as its dominant checkpoint interface.

To rationalize these structure–activity observations and identify the molecular determinants of LAG-3 recognition, the five most active flavonoids (hispidulin, apigenin, isorhamnetin, kaempferol, and luteolin) were docked into a previously identified binding pocket at the D1–D2 interface of human LAG-3 [30], followed by 100 ns molecular dynamics (MD) simulations (Figure 1D). All five protein–ligand complexes remained stable throughout the simulations, with both protein and ligand RMSD values reaching equilibrium after initial relaxation and remaining within a narrow range thereafter (Figure S2). The predicted binding mode was consistent with the experimentally derived flavone pharmacophore: the planar flavone scaffold occupies a shallow cavity at the D1–D2 interface, where the C2=C3 double bond preserves the aromatic character required for favorable C–H···π interactions with Val32. The chromone core is stabilized by contacts with Trp33 and the backbone of Val31, while the 4′-hydroxyl substituent extends deeper into the pocket and interacts with the backbone carbonyl of Pro39 (Figure 1D). Analysis of the MD trajectories showed persistent ligand occupancy and maintenance of these key protein–ligand interactions throughout the simulation. The modeling results also rationalized the observed SAR: hydroxylation of the B ring beyond the 4′ position, as in luteolin and morin, produced favorable docking scores but introduced additional polarity into a predominantly hydrophobic region of the pocket, which may explain why these compounds were experimentally weaker than their docking scores alone would predict. Finally, to evaluate whether this site could recruit apigenin from solution, an additional 200 ns simulation was performed with apigenin initially positioned away from the protein surface. During the trajectory apigenin spontaneously approached the D1–D2

interface, established transient contacts within approximately 10 ns, and progressively converged onto the docking-defined pocket, where it remained stably associated for the remainder of the simulation (Figures S3 and S4). These observations independently support a favorable binding region at the LAG-3 D1–D2 interface and validate the proposed flavone binding mode.

Mapping the apigenin pocket onto the experimentally defined functional epitopes of LAG-3 offers a structural rationale for its checkpoint selectivity. The pocket residues (Val31, Val32, Trp33, Ala34, the Pro39–Pro43 loop, Asp247, and Phe249) are distinct from the residues reported to be required for MHC class II binding (e.g., Asp52, His78, the specificity-determining Tyr99, Arg110, and the Arg125/Asp131/Arg137 cluster) and equally distinct from the D1-loop determinants of FGL1 binding (Val104, Arg113, Gln117, Val120) [6,7,30]. Because apigenin does not directly overlap either ligand-binding footprint, its selective disruption of the LAG-3/MHC-II interaction but not the LAG-3/FGL1 interaction is most consistent with an allosteric mechanism, where by occupying the cleft between the D1 and D2 domains, apigenin is positioned to perturb the conformation or rigidity of the MHC-II–engaging surface, which is contributed by both domains, while leaving the FGL1-binding D1 loop conformationally unaffected. This allosteric model accounts for the functional selectivity observed in the biochemical assays and remains to be confirmed by structure-level analysis of the ternary complexes.

Formulated apigenin restores T-cell activation and functionally synergizes with PD-L1 blockade

To determine whether flavonoid-mediated disruption of the LAG-3/MHCII interaction translates into functional immune activation, we evaluated selected compounds in a cell-based immune checkpoint blockade (ICB) assay. In this system, Jurkat effector cells co-expressing LAG-3 and PD-1 were co-cultured with antigen-presenting surrogate cells expressing MHCII and PD-L1 in the presence of the indicated compounds. Reporter activation was quantified by luminescence as a measure of T-cell signaling. Apigenin, luteolin, and kaempferol induced dose-dependent activation of Jurkat effector cells, reaching levels comparable to the anti-LAG-3 antibody relatlimab at concentrations up to 10 μM (Figure 2A). At higher

concentrations (≥40 µM), though, reporter activity dropped sharply, pointing to compound-associated cytotoxic effects that limit functional interpretation.

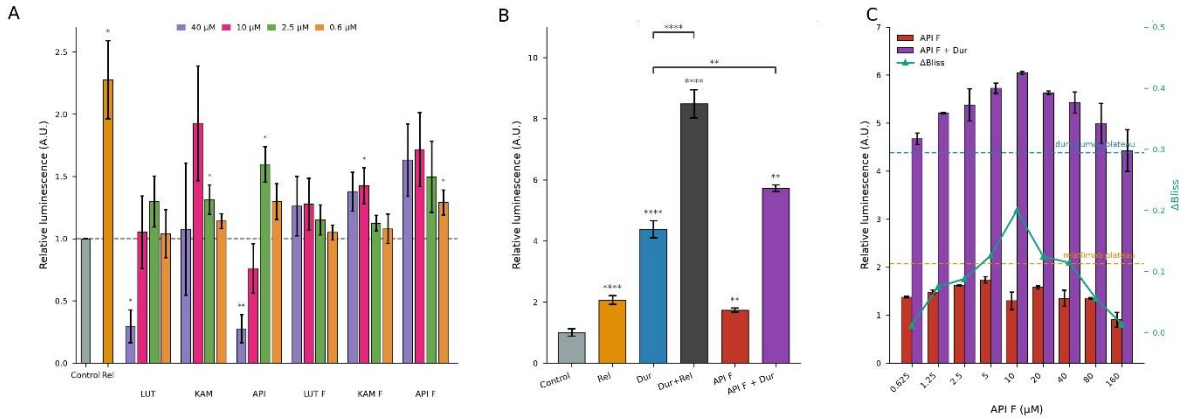


*Figure 2. Formulated apigenin restores checkpoint-dependent T-cell activation and synergizes with PD-L1 blockade.**A** Flavonoid screen in the Jurkat LAG-3/PD-1 reporter assay (n = 3 independent plates, each normalized to its negative control). Free apigenin, luteolin, and kaempferol induce dose-dependent reporter activation at low-to-mid micromolar concentrations but fall below the negative control at 40 µM (free apigenin 0.28 of control), reflecting compound-associated cytotoxicity; Soluplus-formulated compounds (F) maintain activation across the full range. Bars, mean ± SD; asterisks, one-sample t-test versus control (* p < 0.05, ** p < 0.01). Negative control (gray) and relatlimab are shown for reference. **B** Reporter activation for single agents and combinations at 5 µM apigenin. Bars, mean ± SD; asterisks, Welch's t-test versus control (** p < 0.01, **** p < 0.0001); brackets compare the indicated groups to durvalumab alone. **C** Dose-response of formulated apigenin alone and in combination with durvalumab (left axis) with the independently computed Bliss synergy parameter ΔBliss (right axis, teal); dashed lines mark the relatlimab and durvalumab saturation plateaus.*

To mitigate this cytotoxic effect, we evaluated several polymeric formulations, with Soluplus yielding the most favorable outcome. Preparations processed at 50 °C and 6500 PSI displayed a broad amorphous halo and loss of characteristic crystalline peaks in XRD and FTIR analyses, confirming conversion of apigenin into an amorphous solid dispersion (Figure S5–S6; these formulation-characterization data were reported previously in [31]). This transformation improved aqueous solubility and eliminated the decline in reporter signal at higher concentrations, yielding a consistent, extended activation profile, where formulated apigenin, luteolin, and kaempferol each maintained reporter activation above the negative control across the entire concentration range, with formulated apigenin retaining the highest and most consistent activity (Figure 2A). Importantly, apigenin failed to induce reporter activation in the absence of antigen-presenting cells (Figure S7), confirming that its effect depends on checkpoint engagement rather than non-specific T-cell activation.

We next asked whether formulated apigenin could functionally substitute for anti-LAG-3 antibody blockade in combination with PD-L1 inhibition. Durvalumab monotherapy produced strong reporter activation, exceeding LAG-3 blockade with relatlimab alone, and combining relatlimab with durvalumab yielded a further increase, consistent with cooperative dual-checkpoint blockade. This cooperativity mirrors the clinical benefit of combined LAG-3 and PD-1 blockade, as demonstrated by the FDA-approved relatlimab–nivolumab regimen in advanced melanoma [4], supporting the physiological relevance of the reporter system. Because relatlimab and the relatlimab/durvalumab combination represent the maximal attainable reporter output in this assay, they define its saturating upper plateau. As a single agent, formulated

apigenin (5 μM) elicited a significant reporter response that reached approximately 84% of the activity of the anti-LAG-3 antibody relatlimab, a substantial level of activity for a small molecule compared with a therapeutic antibody. Against the assay upper plateau, co-administration of formulated apigenin with durvalumab further increased activation relative to durvalumab alone (Figure 2B). A small molecule thus approached the monotherapy activity of a clinical LAG-3 antibody, although at a considerably higher concentration and, in combination with PD-L1 blockade, recovered a substantial fraction of the dual-antibody response.

To determine whether this interaction was synergistic, we applied the Bliss independence model, computed directly from the raw luminescence data using the dual-checkpoint (relatlimab + durvalumab) response as the upper plateau. Observed combination responses exceeded the predicted additive effect at every tested concentration, yielding uniformly positive ΔBliss values that peaked at 10 μM (ΔBliss ≈ 0.20, Figure 2C). Across the ascending dose range the combination remained above the durvalumab saturation plateau, and both apigenin and the apigenin/durvalumab combination reached half-maximal activation at sub-micromolar concentrations (EC_{50} ~1 μM), so the synergistic effect is engaged at pharmacologically accessible doses.

To confirm that the drop in reporter signal at higher concentrations reflected the intrinsic activity upper plateau rather than residual toxicity, we performed parallel viability assays under identical conditions. In contrast to the unformulated compound, formulated apigenin preserved cell viability across the entire concentration range (≥85% at all doses tested, including 160 μM, Figure S8). The high-dose roll-off in reporter signal therefore occurs under fully viable conditions and reflects the saturable nature of checkpoint-dependent activation rather than cytotoxicity. Within a non-cytotoxic concentration range, formulated apigenin substituted for anti-LAG-3 antibody and cooperated with PD-L1 blockade, recovering a substantial fraction of the dual-checkpoint response with a small molecule rather than a second antibody.

Apigenin directly engages LAG-3 in a cellular context

To validate target engagement in a cellular context, we synthesized a photoactivatable apigenin probe bearing a diazirine group for UV-induced covalent crosslinking and a terminal alkyne for click-chemistry enrichment (Figure 3A). Jurkat cells co-expressing LAG-3 and PD-1 were incubated with the probe and irradiated with UV light to covalently capture apigenin-bound proteins in situ. Cells were washed and lysed, a biotin tag was conjugated to the alkyne handle by click chemistry, and labeled proteins were enriched on streptavidin beads, digested, and identified by LC–MS/MS (Figure 3B).

Quantitative comparison of apigenin-probe versus vehicle (DMSO) pull-downs identified LAG-3 as the most strongly and significantly enriched protein among quantified proteins (Figure 3C). LAG-3 was captured almost exclusively in the apigenin-probe condition, undetectable across all vehicle replicates yet consistently recovered in the probe pull-down. Its identification in unfractionated whole-cell lysates

provides unbiased evidence that apigenin may engage LAG-3 in its native cellular environment rather than acting only through the indirect or pathway-level mechanisms previously described. A small number of additional proteins, including RNH1, ARID1B, PSMA7, PSMB1, KPNB1, and HSP90AA1, were also enriched but at substantially lower magnitude, consistent with the secondary or nonspecific interactions commonly observed in photoaffinity-labeling experiments.

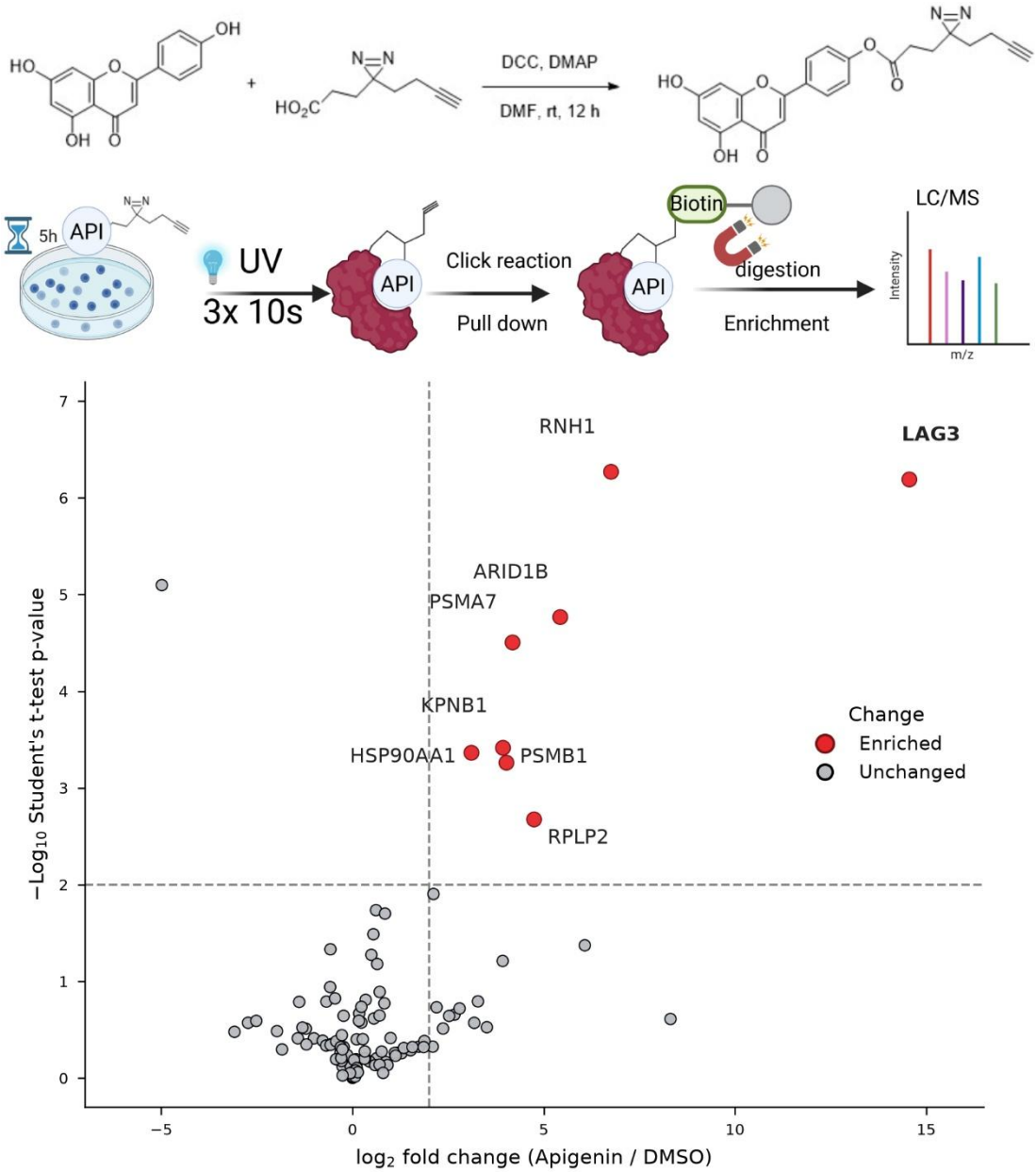


Figure 3. Apigenin directly engages LAG-3 in intact cells by photoaffinity chemoproteomics. (A) The synthesis scheme of the photoactivatable apigenin probe, bearing a diazirine group for UV-induced covalent crosslinking and a terminal alkyne for click-chemistry enrichment. (B) Workflow: LAG-3/PD-1–expressing Jurkat cells were incubated with the probe and UV-irradiated to covalently capture apigenin-bound proteins. After lysis, a biotin tag was appended to the alkyne by click chemistry, and labeled proteins were enriched on streptavidin beads, digested, and identified by LC–MS/MS. (C) Volcano plot of apigenin-probe versus vehicle (DMSO) pull-downs (n = 2 probe, n = 3 vehicle); the x-axis shows the log2 fold change (apigenin/DMSO) and the y-axis the −log10 p-value. LAG-3 is the most strongly and significantly enriched of 114 quantified proteins.

Apigenin and PD-L1 blockade cooperatively activate primary human T cells

To assess whether apigenin-mediated LAG-3 modulation translates to primary human immune cells, we evaluated its activity in peripheral blood mononuclear cells (PBMCs) isolated from healthy donors. To ensure sufficient LAG-3 expression, PBMCs were first stimulated with anti-CD3 antibody, which induced strong upregulation of LAG-3 on both $CD4^+$ and $CD8^+$ T-cell populations (Figure S9). Cells were subsequently co-cultured with antigen-presenting surrogate cells expressing MHCII and PD-L1 in the presence of formulated apigenin, durvalumab, or the combination.

Under these conditions, which model a highly activated T-cell environment, apigenin monotherapy had only modest effects on activation markers, consistent with the elevated baseline induced by anti-CD3 stimulation. Durvalumab alone also produced moderate activation, primarily within the $CD4^+$ compartment. Co-administration of formulated apigenin with durvalumab, however, resulted in a statistically significant increase in the early activation marker CD69 on $CD4^+$ T cells and the late activation marker CD137 on $CD8^+$T cells (Figure 4). This pattern points to coordinated activation across T-cell subsets, with increased helper T-cell priming and cytotoxic T-cell activation. In line with this, combination treatment significantly increased IFN-γ production in $CD4^+$ T cells relative to control (Figure 5A). In $CD8^+$ T cells, apigenin alone induced a significant increase in IFN-γ expression relative to control, while the addition of durvalumab did not further increase this response (Figure 5B). The magnitude of these effects should be interpreted in the context of the experimental system, where anti-CD3 stimulation establishes a highly activated baseline required for LAG-3 expression, which compresses the dynamic range of additional checkpoint-mediated responses. In addition, the known anti-inflammatory properties of apigenin may limit excessive cytokine production while preserving checkpoint-dependent signaling [32].

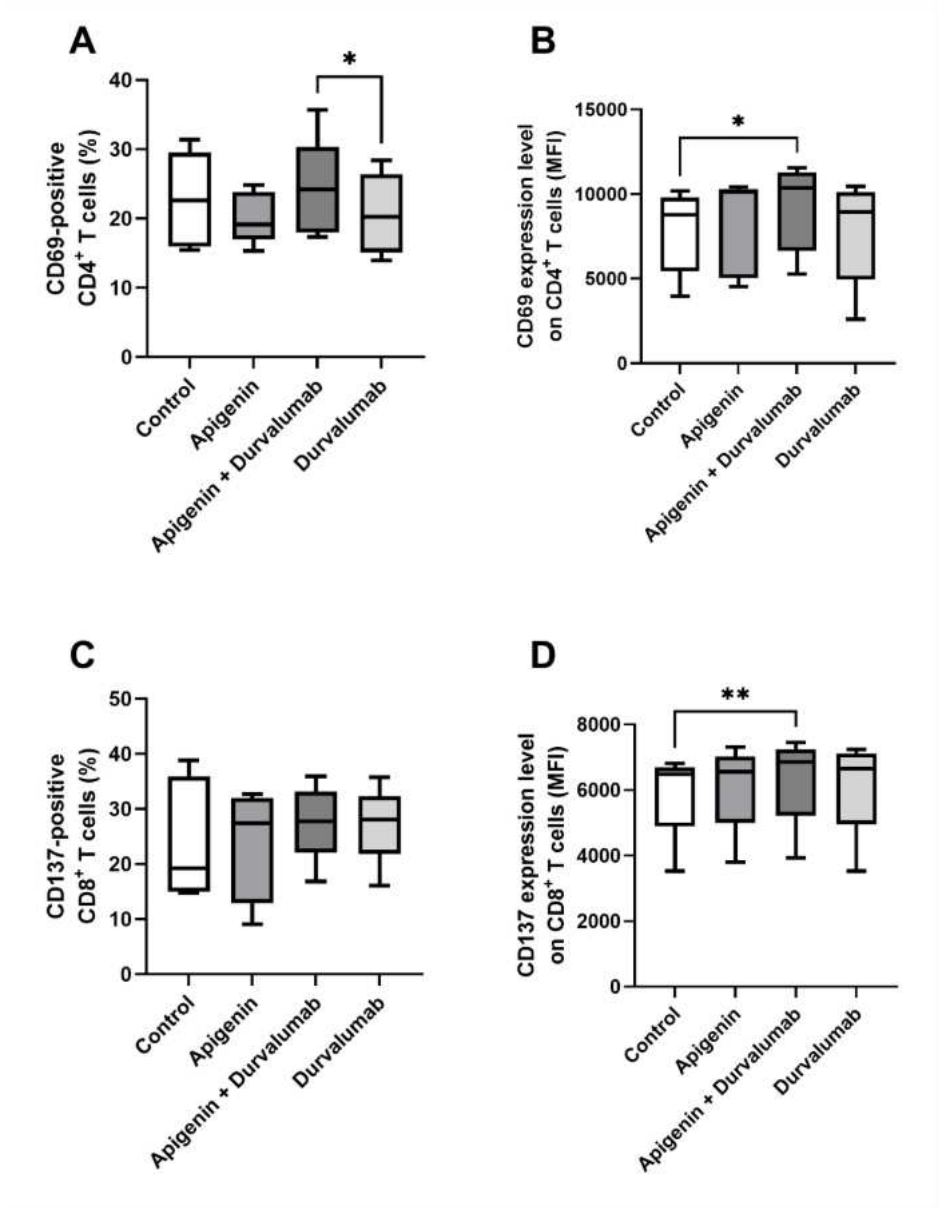


*Figure 4. Expression of activation markers on CD4+ and CD8+ T cells from healthy donor PBMC samples cultured with APC cells and treated with apigenin and/or durvalumab. CD69 expression on CD4+ T cells was analyzed as the percentage of cells expressing CD69 activation marker (A) or the expression level based on MFI (B). CD137 expression on CD8+ T cells was analyzed as the percentage of cells expressing CD137 activation marker (C) or the expression level based on MFI (D). Experiment was performed using PBMC samples isolated from five different heathy blood donors. Data was analyzed using Freidmann paired test with Dunn's correction and median with IQR is shown. Asterisks mark significant differences: **p<0.01, *p<0.05.*

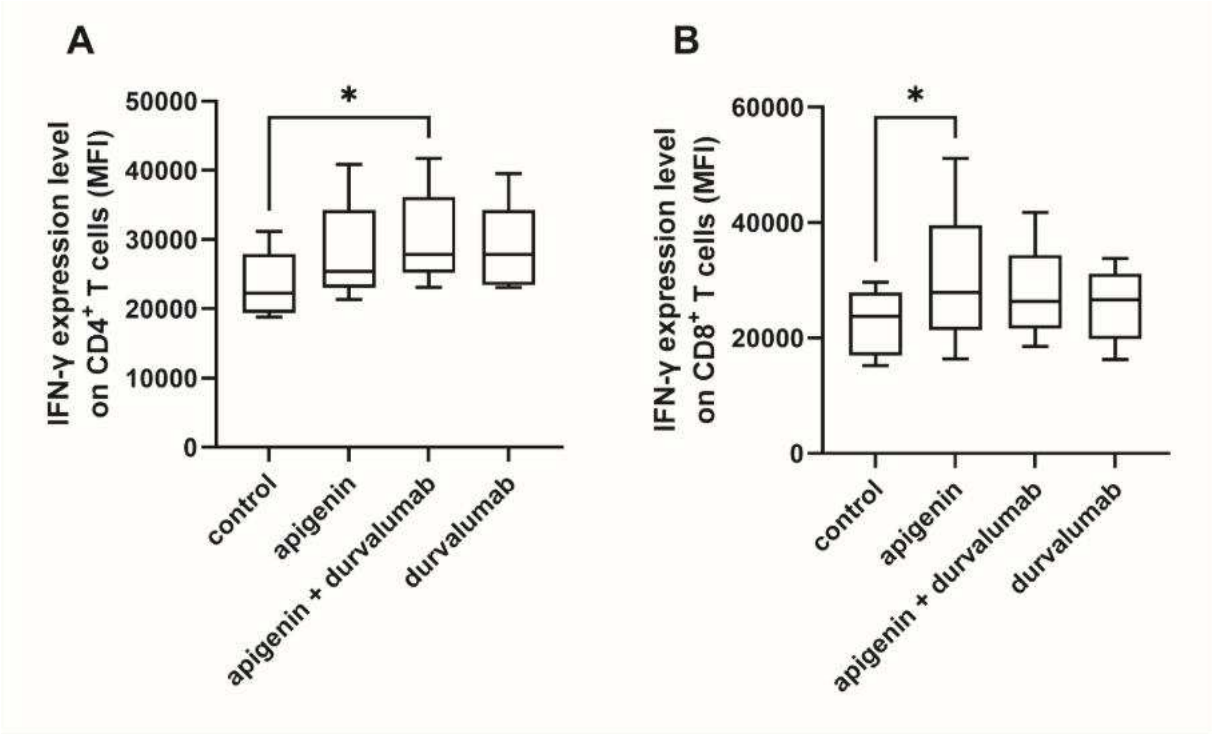


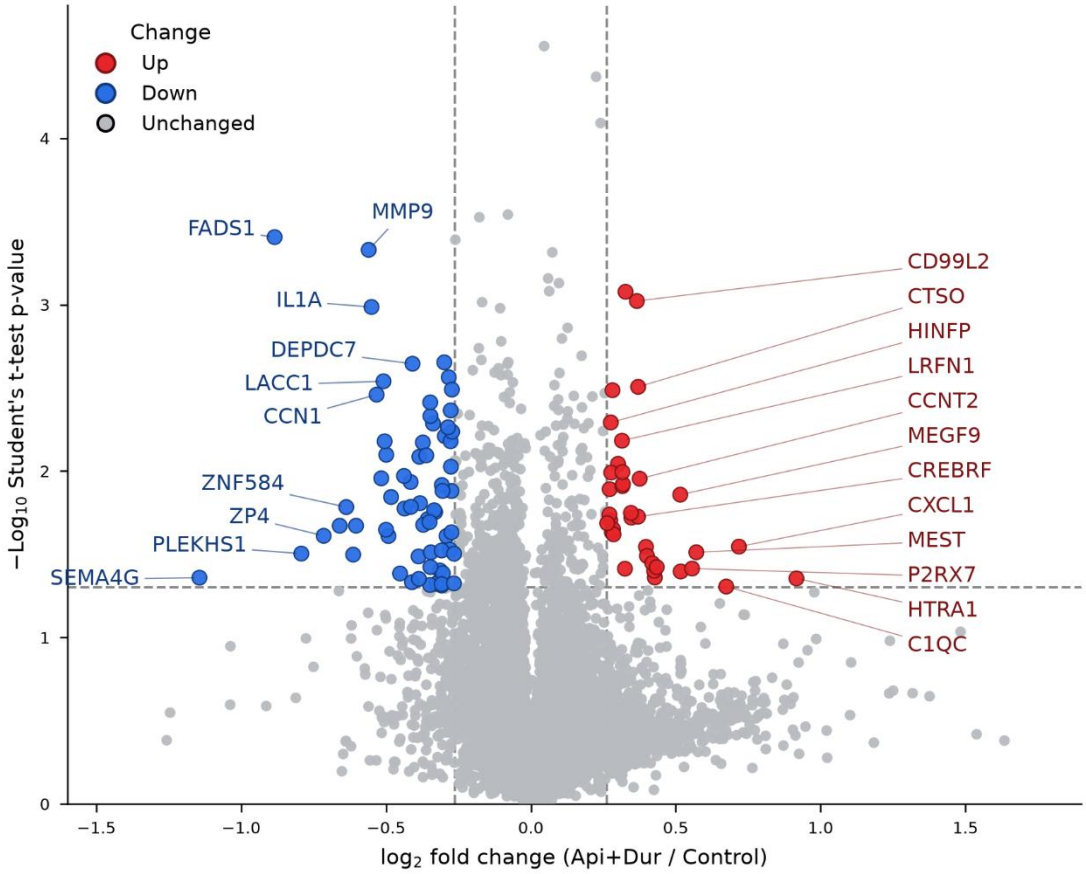
*Figure 5. IFN-γ production in CD4+ and CD8+ T cells from healthy donor PBMC samples cultured with APC cells and treated with apigenin and/or durvalumab. IFN-γ production was analyzed in CD4+ (A) and CD8+ T cells based on MFI level. Experiment was performed using PBMC samples isolated from five different heathy blood donors. Data was analyzed using Freidmann paired test with Dunn's correction and median with IQR is shown. Asterisks mark significant differences: *p<0.05.*

Combination therapy alters immune signaling and tissue-interaction programs in T cells

To investigate the molecular consequences of combined LAG-3 and PD-L1 blockade, we performed quantitative proteomic profiling of primary human T cells following co-culture with MHCII- and PD-L1-expressing surrogate antigen-presenting cells in the presence of formulated apigenin and durvalumab or vehicle control. Differential protein abundance analysis showed distinct changes in immune signaling and tissue-interaction pathways (Figure 6A). Among the upregulated proteins, GO enrichment analysis identified pathways related to neutrophil extravasation, leukocyte migration, and lymphocyte migration. Immune response and interleukin-1–regulated signaling pathways were also enriched. At the protein level, ORAI3, SDC4, and ITPRIPL1 increased in abundance, consistent with changes in calcium-dependent and membrane-proximal signaling. P2RX7 and CXCL1 levels were also elevated, along with metabolic and stress-associated proteins such as SESN2 and DHRS1. Other upregulated factors included transcriptional and signaling regulators such as CEBPD, CCNT2, CLK1, and CLK4, along with proteins involved in adhesion and membrane trafficking, including SDC4, CD99L2, SDF4, and ATP9B.

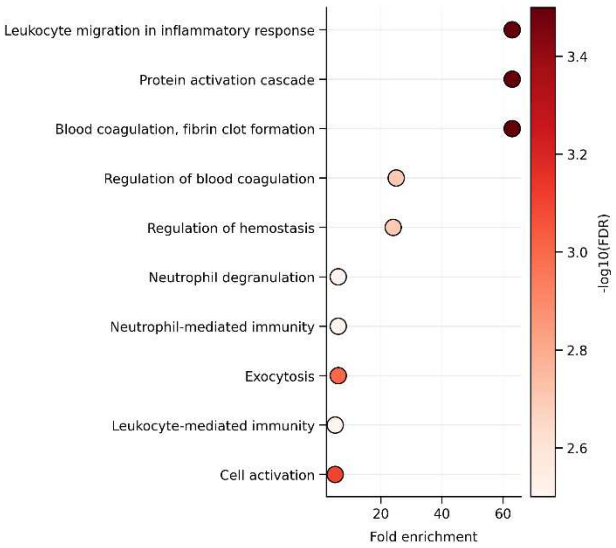
In contrast, the downregulated proteome showed a coherent suppression of extracellular matrix organization and developmental plasticity programs. GO enrichment showed a reduction of pathways associated with extracellular matrix and structural organization, as well as cell migration, mesenchymal differentiation, and

broader morphogenetic and neural crest–related developmental processes. This pattern suggests attenuation of stromal remodeling and tissue architecture programs that are frequently associated with immune exclusion and tumor progression. At the protein level, reduced expression of MMP9 and the collagen crosslinking enzymes LOXL3 and LOXL4 indicated decreased extracellular matrix remodeling capacity, while downregulation of SPHK1 and S1PR2 suggested suppression of sphingolipid signaling pathways linked to impaired immune cell migration and dysfunction. Additional reductions in CSF1 and IL1A pointed to diminished myeloid recruitment and inflammatory modulation, and decreased SEMA3A and ADM further supported relief from inhibitory guidance and tumor-supportive signaling programs.



GO Biological Process Enrichment Following Combined LAG-3 and PD-L1 Blockade

Upregulated proteins



Downregulated proteins

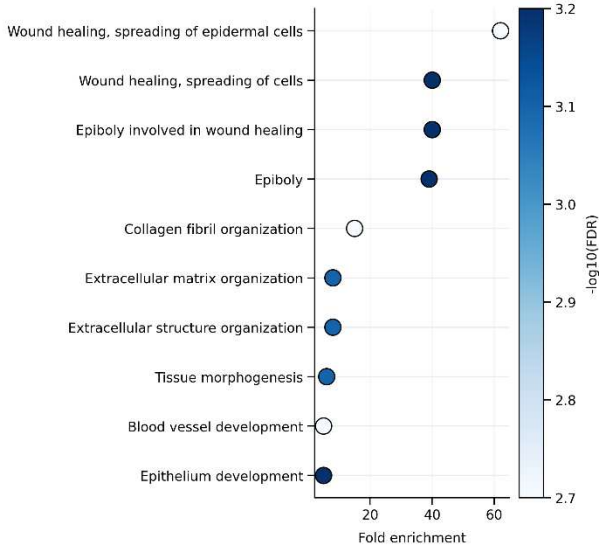




*Figure 6. Combination of formulated apigenin and durvalumab reshapes the T-cell proteome. Primary human T cells were co-cultured with MHCII/PD-L1 antigen-presenting surrogate cells in the presence of formulated apigenin plus durvalumab (API+DUR) or vehicle (CON), and analyzed by quantitative mass spectrometry (n = 4). (A) Volcano plot of the API+DUR versus CON comparison. Red, significantly up-regulated proteins ($p < 0.05$, fold change > 1.2); blue, significantly down-regulated proteins ($p < 0.05$, fold change < −1.2); grey, unchanged. The x-axis shows the Student's t-test difference (log2 fold change) and the y-axis the −log10 p-value; immunoglobulins were excluded to improve visualization. Selected proteins are labeled. (B–C) Gene Ontology enrichment of the up-regulated (B) and down-regulated (C) protein sets. (D) Individual protein intensities (log2) in control versus apigenin-treated T cells for representative significantly regulated proteins (n = 4; boxes show median and interquartile range). Asterisks mark significant differences by Student's t-test: *p < 0.05, **p < 0.01, ***p < 0.001.*

Combination of apigenin and PD-L1 blockade enhances antitumor efficacy in vivo

To determine whether the observed in vitro effects translate into antitumor activity in vivo, we evaluated formulated apigenin in combination with PD-L1 blockade in a syngeneic model. C57BL/6 mice bearing subcutaneous PD-L1–humanized MC38 colon carcinoma were randomized (n = 5) when tumors reached approximately 50 mm^3 to vehicle (1% DMSO in PBS), durvalumab (2.5 mg/kg intravenously, twice weekly), formulated apigenin (100 mg/kg/day by oral gavage), or the combination, and treated for 15 days. Tumors in the vehicle group progressed rapidly, while both monotherapies slowed tumor growth (Figure 7A). Durvalumab produced a tumor growth inhibition (TGI) of 59.2% (terminal tumor volume 247.17 ± 63.84 mm^3, weight 0.53 ± 0.17 g) and apigenin a TGI of 44.4% (334.35 ± 100.20 mm^3, 0.72 ± 0.10 g). The combination was most effective, producing the lowest terminal tumor burden and a TGI of 77.7% (calculated from terminal tumor weight, 228.79 ± 46.40 mm^3, 0.29 ± 0.11 g). On the growth curve, the combination and durvalumab tracked closely, both suppressing tumor progression relative to vehicle and to apigenin monotherapy (Figure 7A). The combination's advantage over durvalumab was most evident in the terminal excised-tumor weight, which was significantly lower than both vehicle and durvalumab (Figure 7B, C). Body weight remained stable across all groups, indicating that both monotherapies and the combination were well tolerated (Figure 7D).

Flow-cytometric profiling of tumor-infiltrating lymphocytes (CD3/CD4/CD8 panel) showed that combination therapy produced the highest frequency of intratumoral CD8+T cells, which rose from approximately 8.1% of the gated population in the vehicle group to 26.5% with durvalumab, 19.1% with apigenin, and 32.9% with the combination (Figure 7E). A similar but more moderate pattern was observed in peripheral blood, where the CD8+T-cell frequency increased from approximately 9.8% (vehicle) to 17.8% (durvalumab), 13.7% (apigenin), and 20.7% (combination). These data indicate that apigenin co-administration increases both systemic and intratumoral cytotoxic T-cell representation beyond the level achieved by PD-L1 blockade alone.

To determine whether the combination increased cytolytic effector function within the tumor, the cytotoxic-effector markers granzyme B and perforin were assessed in tumor sections by immunohistochemistry. Both markers, which together

report the granule-exocytosis pathway used by cytotoxic T lymphocytes and natural killer cells to kill target cells, were increased by the apigenin–durvalumab combination relative to control and either monotherapy (Figure 7F, G), indicating greater intratumoral cytotoxic potential under the combined regimen.

To characterize tolerability, a standard histopathological assessment of heart, liver, spleen, lung, and kidney was performed at the end of the study. H&E staining revealed no overt morphological abnormalities in any examined organ across treatment groups (Figure S10), and serum chemistry showed no evidence of hepatotoxicity or nephrotoxicity. These data support a model in which formulated apigenin plus durvalumab increases immune-mediated tumor-cell killing while maintaining a favorable safety profile, supporting further translational development of this combination.

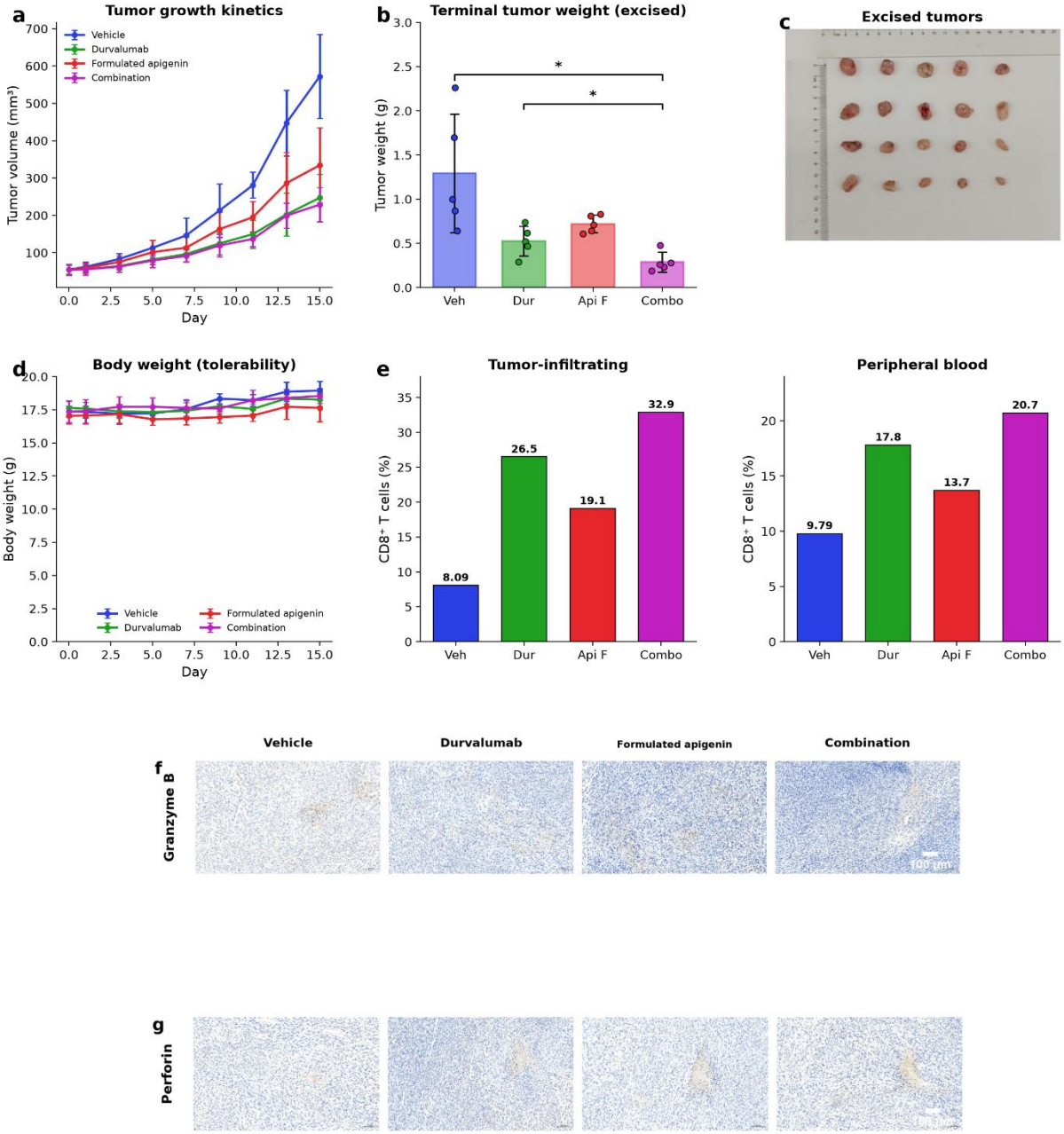


Figure 7. ***Apigenin plus durvalumab enhances antitumor efficacy in vivo.*** C57BL/6 mice bearing PD-L1–humanized MC38 tumors were treated with vehicle, durvalumab, formulated apigenin, or the combination (n = 5 per group). (a) Tumor growth kinetics over the 15-day treatment period (caliper volume; mean ± s.d.). (b) Terminal excised-tumor weight with individual animals overlaid; brackets denote comparisons by Welch's t-test (vehicle vs combination, p = 0.027; durvalumab vs combination, p = 0.033). The combination separated from durvalumab on this gravimetric endpoint but not on the caliper growth curve in (a), consistent with terminal tumor weight being the more precise measure of tumor burden. (c) Photograph of excised tumors at study endpoint. (d) Body weight over time as a tolerability measure (mean ± s.d.). (e) Frequency of $CD8^+$ T cells (percentage of the gated population) among tumor-infiltrating and peripheral-blood lymphocytes by flow cytometry, shown as representative values per group. (f, g) Representative immunohistochemistry of intratumoral granzyme B (f) and perforin (g); scale bar, 100 µm. Tumor growth inhibition (TGI), calculated from terminal tumor weights, was 59.2% (durvalumab), 44.4% (formulated apigenin) and 77.7% (combination).

Discussion

The present study identifies apigenin as a small-molecule modulator of the LAG-3 immune checkpoint and demonstrates that it synergizes with PD-L1 blockade to increase T-cell activation and antitumor immunity. Using complementary biochemical, modelling, chemoproteomic, cellular, and in vivo approaches, we establish LAG-3 as a direct molecular target of apigenin and show that combined treatment with durvalumab recapitulates key features of dual checkpoint inhibition.

Recent clinical advances have shown the therapeutic value of simultaneously targeting LAG-3 and PD-1/PD-L1 pathways, as exemplified by the approval of relatlimab in combination with nivolumab. These findings support a model in which LAG-3 and PD-1/PD-L1 mediate non-redundant inhibitory programs in exhausted T cells. In line with this concept, pan-cancer analysis of TCGA cohorts, using tumor purity–adjusted partial Spearman correlations, revealed strong co-variation of LAG-3 with both PD-1 and PD-L1, most pronounced within T cell–inflamed ("hot") tumor microenvironments and weakest or absent in immunologically "cold" cohorts (Figure 8). Across nearly all tumor types the association of LAG-3 with PD-1 exceeded that with PD-L1. This reflects their shared expression on chronically stimulated T cells, while PD-L1 is more broadly regulated by tumor- and microenvironment-derived cues. This co-expression architecture gives a mechanistic basis for combined checkpoint targeting.

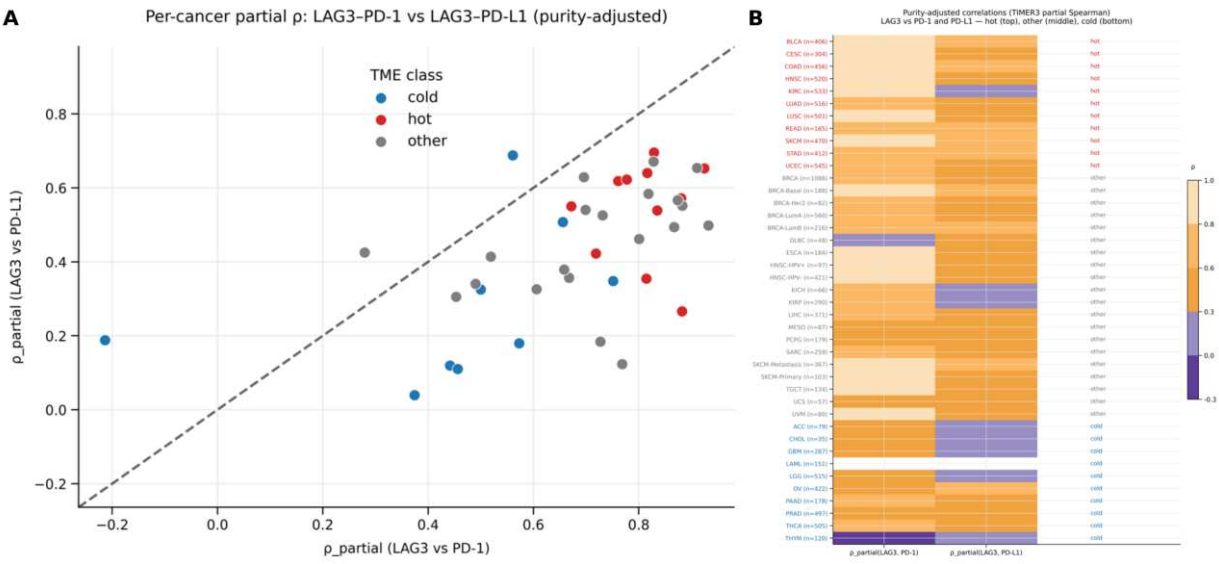


Figure 8. LAG3 co-expression with PD-1 and PD-L1 across human cancers. Tumor purity–adjusted partial Spearman correlations (TIMER3) between LAG-3 and PD-1) or PD-L1 were computed for TCGA cohorts. (A) Per-cancer comparison of the LAG-3–PD-1 correlation (x-axis) against the LAG-3-PD-L1 correlation (y-axis); each point is one cohort, colored by tumor-microenvironment class (hot, cold, other). Points falling below the dashed line of identity indicate a stronger LAG-3-PD-1 than LAG-3–PD-L1 association. (B) Heatmap of the same two correlations for each cohort (sample sizes in parentheses), grouped by microenvironment class. Warm colors denote positive correlation; cohorts are ordered hot (top), other (middle), and cold (bottom).

Within this framework, we show that apigenin directly engages LAG-3 in a cellular context and disrupts the LAG-3/MHCII interaction without detectable activity

against the PD-1/PD-L1 or LAG-3/FGL-1 axis. Functional assays further show that formulated apigenin increases PD-L1 mediated T-cell blocade activation across reporter systems, primary human T cells, and in vivo models, supporting its role as a small-molecule functional counterpart to antibody-based LAG-3 inhibition.

Previous studies have attributed the immunomodulatory effects of apigenin mainly to indirect mechanisms, including STAT1-dependent suppression of PD-L1 expression in tumor and immune cells [17,18]. Such effects likely contribute to its pleiotropic activity, but our data define an additional, mechanistically distinct mode of action, in which apigenin directly targets LAG-3 at the receptor level. These mechanisms are not mutually exclusive and may act together to amplify checkpoint modulation. As a pleiotropic dietary flavone, apigenin may engage additional targets. Nonetheless, LAG-3 was the dominant protein captured in pull-downs, and appropriate formulation was essential to unmask this checkpoint-directed activity. This study also re-evaluates apigenin under conditions that eliminate confounding effects of poor solubility and nonspecific cytotoxicity, which have historically complicated interpretation of polyphenol activity in cancer models. By using a formulation that improves solubility and preserves cell viability at active concentrations, we isolated checkpoint-specific effects and revealed direct immunoregulatory activity that may have been previously obscured by stress-related artifacts.

Consistent with these findings, quantitative proteomic profiling showed that combined apigenin and PD-L1 blockade produces a coordinated immune-stromal reprogramming in T cells. Upregulated pathways were dominated by immune activation and leukocyte trafficking programs, including neutrophil and lymphocyte migration, interleukin-1–regulated signaling, and immune response activation, reflecting greater inflammatory responsiveness and immune cell recruitment capacity. Downregulated pathways, in turn, were significantly enriched in extracellular matrix organization, structural remodeling, and developmental programs associated with tissue plasticity and immune exclusion. These changes define a bidirectional shift toward an immune-activated and less structurally restrictive cellular state, consistent with greater antitumor immune activity.

These molecular signatures are mirrored at the functional level, where combined treatment increases the frequency of CD8+T cells within tumors and in peripheral blood and increases granzyme B and perforin expression, indicating strengthened cytotoxic effector function in vivo. Correspondingly, tumor growth inhibition is significantly greater under combination therapy than either monotherapy alone.

These findings establish LAG-3 as a direct small-molecule target of apigenin and show that pharmacological modulation of this checkpoint can synergize with PD-L1 blockade to increase antitumor immunity. Beyond providing a mechanistic basis for apigenin activity, this work shows the feasibility of small-molecule targeting of inhibitory immune receptors traditionally considered accessible only to biologics. Future work will focus on defining the structural basis of apigenin–LAG-3 interaction and optimizing this

scaffold for improved potency and selectivity, enabling rational development of orally available checkpoint modulators for combination immunotherapy.

Conclusions

This work identifies the dietary flavone apigenin as a direct small-molecule inhibitor of LAG-3. A flavone structure–activity relationship first pinpointed apigenin as the effective disruptor of the LAG-3/MHCII interaction, and orthogonal biophysical and pull-down assays confirmed direct target engagement. Once formulated to overcome its poor solubility and nonspecific cytotoxicity, apigenin restored checkpoint-dependent T-cell activation and, in combination with the PD-L1 antibody durvalumab, enhanced immune activation across reporter assays, primary human T cells, and a humanized in vivo mice tumor model, where the combination produced the greatest tumor growth inhibition and the strongest cytotoxic effector response. Together, these findings establish LAG-3 as a druggable small-molecule target and position apigenin as a functional counterpart to antibody-based LAG-3 blockade that can be combined with approved PD-L1 inhibitors. More broadly, they demonstrate that inhibitory immune receptors long considered accessible only to biologics can be modulated pharmacologically by small molecules, opening a path toward orally available checkpoint-targeting agents and rationally designed combination immunotherapies.

Materials and Methods

Materials

All active compounds tested in HTRF assay were purchased from Medchem Express.

HTRF binding assays

The LAG-3/MHCII and PD-1/PD-L1 HTRF assays were performed using a certified Revvity assay kit, and the LAG-3/FGL1 HTRF assay was performed using a certified BPS Bioscience assay kit, following the respective standard protocols. Measurements were carried out on two independent dilution series to determine the half-maximal inhibitory concentration (IC_{50}) of the tested compounds. FRET measurements were recorded using a Tecan Spark 20M plate reader. The collected data were background-subtracted using the negative control, normalized to the positive control, averaged, and fitted using a normalized Hill equation to determine IC_{50} values in Mathematica 12. For compounds for which IC_{50} values could not be determined, a “dissociation value” (defined as the percentage of the undissociated LAG-3/MHCII or LAG-3/FGL1 complex) at a concentration of 50 μM is reported.

Cell-based immune checkpoint blockade (reporter) assay

A cell-based immune checkpoint blockade bioassay (Promega) was used to verify blockade of the LAG-3/MHCII and PD-1/PD-L1 interactions in vitro by selected small-molecule inhibitors. Antigen-presenting cells (APCs) overexpressing MHCII and PD-L1 were maintained in DMEM supplemented with 10% FBS, and Jurkat effector cells

(Jurkat-EC) co-expressing LAG-3 and PD-1 were maintained in RPMI-1640 with 10% FBS. APCs were seeded in white opaque 96-well plates at 15,000 cells in 100 µL per well of growth medium (DMEM with 10% FBS). 4-fold serial dilutions of the inhibitors were prepared in DMSO (BioShop) and diluted 1,000-fold in assay buffer (RPMI-1640 with 1% FBS), keeping the final DMSO concentration at 0.05% (v/v) in all samples. DMSO served as the negative control, while durvalumab (anti-hPD-L1 monoclonal antibody, Selleckchem; 5 µg/mL final) and relatlimab (anti-hLAG-3 monoclonal antibody; 5 µg/mL final) served as positive controls, whose activation of Jurkat-ECs was set to 100%. Seventeen hours after seeding, the medium was harvested, and 40 µL of the serial compound dilutions or of the negative or positive control was added per well. A co-culture was then established by adding Jurkat effector cells at 20,000 cells in 40 µL per well, and was maintained at 37 °C and 5% CO_2 for 6 h. Plates were equilibrated to room temperature for 10 min and incubated with Bio-Glo assay reagent (Promega; 75 µL per well) for 20 min at room temperature. Effector-cell activity was determined by measuring luminescence on a Spark microplate reader (Tecan). Data were expressed as the percentage of maximum checkpoint blockade, where 0% corresponds to DMSO-treated Jurkat-ECs and 100% to activation by the reference antibody at 5 µg/mL. Data points represent mean ± standard deviation from three independent experiments, each performed in duplicate. Where applicable, EC_{50} values were determined by fitting a Hill curve to the data in OriginPro 2024b (OriginLab).

Cell viability (Biolog Redox Dye) assay

Jurkat effector cells (Jurkat-EC), switched 24 h earlier to RPMI-1640 medium with 1% FBS, were seeded into transparent 96-well plates at 20,000 cells in 40 µL per well. Four-fold serial dilutions of the small-molecule inhibitors were prepared in DMSO and diluted 1,000-fold in culture medium (RPMI-1640 with 1% FBS), and cells were treated with 40 µL per well. DMSO (0.05% (v/v) final) served as the control. Plates were incubated for 48 h at 37 °C and 5% CO2, after which the tetrazolium reagent Biolog Redox Dye MIX MB (Biolog) was added for 4 h to a final concentration of 500 µM per well. Absorbance was measured at 590 nm, with 750 nm as reference, on a Spark microplate reader (Tecan). Data points represent the mean survival rate of Jurkat-ECs ± standard deviation relative to DMSO-treated cells, from three independent experiments each performed in duplicate, and were plotted in GraphPad Prism version 8.0.1.

Microscale thermophoresis (MST)

Recombinant LAG-3 (MedChemExpress) was fluorescently labelled on its histidine tag using the His-tag labelling kit (NanoTemper), in accordance with the manufacturer's protocol. Binding of apigenin was measured by spectral shift on a Dianthus instrument (NanoTemper): a serial dilution of apigenin was prepared in assay buffer containing 1% (v/v) DMSO, and the ratio of fluorescence emission at 670 and 650 nm was recorded across three independent dilution series (Figure S1D). The apparent dissociation constant (Kd ≈ 15 µM) was determined from the midpoint of the spectral-shift binding transition (plateau-midpoint construction).

Molecular docking and modeling

The model of hLAG-3 (PDB 9BF9 template) and the initial conformations of the selected flavonoids were prepared in the Maestro 13.4 suite for the molecular docking purpose. Hydrogen atoms in the idealized positions were added to the protein structure. The energy of ligands was minimized using the OPLS4 Force Field. Molecular docking simulations were performed using GOLD 2021.3.0 (Genetic Optimization for Ligand Docking) software [33]. The docking sphere was set to 25 Å radius with the center set at F249, corresponding to the binding site identified in our previous virtual-screening studies. The number of GA runs was set to 10 for each molecule and for each generated pose the ChemPLP scoring function was calculated[34]. Results were visualized and analyzed using PyMOL .

The stability of the predicted protein-ligand complexes was evaluated by molecular dynamics (MD) simulations were performed using GROMACS 2021.3 software[35]. The CHARMM36 Force Field [36] and the CHARMM General Force Field was used for protein and ligands, respectively. The rhombic dodecahedron box was selected, and the system was solvated using TIP3P model [37] for water treatment. The Cl- counter ions were applied to neutralize systems. The energy minimalization, equilibration and MD runs were performed at 37°C and 1.0 bar. The total time of simulations was set at 100 ns and 200 ns (depending on simulation), with 2 fs step. The analysis of the trajectories was performed with GROMACS native tools. PyMOL was used to analyze and visualize recorded trajectories.

PBMC isolation and culture

Peripheral blood mononuclear cells (PBMC) were isolated by standard density-gradient centrifugation using Pancoll human (PAN-Biotech, Aidenbach, Germany). Anticoagulated citrate-dextrose-A-treated blood from healthy donors was purchased from the Regional Centre of Blood Donation and Blood Therapy in Krakow, Poland. PBMC were cultured in DMEM medium (PAN-Biotech) supplemented with 10% (v/v) heat-inactivated fetal bovine serum (FBS; Diagnovum, Greifswald, Germany) and 1% (v/v) penicillin-streptomycin (PAN-Biotech) at 37°C and 5% CO_2. For LAG-3 expression, PBMC were stimulated with purified anti-human CD3 (BD Pharmingen) at 1 µg/mL for 24 h at 37 °C and 5% CO_2.

PBMC and APC co-culture

To analyze the influence of apigenin and durvalumab on PBMC activation and function, PBMC were added to antigen-presenting cells (APC) seeded 24 h in advance in 24-well plates. Apigenin and/or durvalumab was then added for a 24 h co-culture, or cells were left untreated. For cytokine-expression analysis, cells were additionally stimulated for 24 h with a 1× cocktail of phorbol 12-myristate 13-acetate (PMA) and ionomycin (Cell Stimulation Cocktail, eBioscience, Thermo Fisher Scientific, San Diego, CA, USA) in the presence of a 1× cocktail of Brefeldin A and monensin (Protein Transport Inhibitor Cocktail, eBioscience). After culture, PBMC were collected and washed twice with PBS.

Flow cytometry

The following mouse monoclonal antibodies (mAbs) against human molecules were used: anti-CD4-FITC (clone RPA-T4), anti-CD8a-PerCP-Cy5.5 (clone RPA-T8), anti-CD69-PE (clone FN50), anti-HLA-DR-PE-Cy7 (clone LN3), anti-CD137-Alexa Fluor 700 (clone 4B4), anti-CD25-APC (clone CD25-4E3), anti-LAG-3-APC (clone 3DS223H), anti-IL-2-APC (clone MQ1-17H12), anti-IFN-γ-PE-Cy7 (clone 4S.B3), and anti-TNF-α-Alexa Fluor 700 (clone MAb11) (all Invitrogen), together with appropriate isotype controls. For cell-surface staining, PBMC were incubated with mAbs for 20 min at 4 °C, washed twice, resuspended in PBS, and analyzed on a CytoFLEX flow cytometer (Beckman Coulter). Intracellular staining of TNF-α, IFN-γ, and IL-2 was performed after PMA/ionomycin stimulation in the presence of Brefeldin A and monensin; cells were fixed and permeabilized using the Intracellular Fixation & Permeabilization Buffer Set (Invitrogen) according to the manufacturer's protocol, washed twice with PBS, incubated with intracellular-staining mAbs for 30 min at 4 °C, washed, and analyzed on the CytoFLEX cytometer. Data were analyzed with Kaluza Analysis software (Beckman Coulter), expression was reported as the percentage of positively stained cells and the mean fluorescence intensity (MFI).

Proteomics: sample preparation and measurement

Cell lysates were sonicated twice for 5 min using a 30 s/30 s ON/OFF cycle in a Bioruptor Pico (Diagenode), then centrifuged, and the supernatants collected. Protein samples (20 µg, cell lysates as well as chemoproteomic pull-down samples) were prepared for LC-MS/MS analysis using the SP3 protocol (Hughes et al., 2018). The resulting peptides were suspended in 0.1% formic acid (FA) and 250 ng of the peptide mixture was analyzed on an Orbitrap Astral mass spectrometer coupled to a Vanquish Neo UHPLC (both Thermo Fisher Scientific) operated in direct-injection mode. Peptides were separated on an Aurora Ultimate XT 25 cm × 75 µm C18 column (IonOpticks) using a 60 min acetonitrile (ACN) gradient at 0.5 µL/min and 55 °C. The gradient consisted of three steps: 2–10% B over 10 min, 10–25% B over 32 min, and 25–45% B over 18 min (buffer B: 80% ACN, 0.1% FA; buffer A: 0.1% FA). Eluting peptides from cell lysate samples were analyzed by a data-independent acquisition (DIA) method, collecting 200 windows of 3 Th for precursors in the 380–980 m/z range. The maximum injection time (IT) was 5 ms and the normalized AGC target 500%; isolated ions were fragmented at a normalized collision energy of 25%. The Astral scan range was 150–2000 m/z. Full-MS spectra were acquired every 0.6 s at a resolution of 240,000 over 380–980 m/z with a maximum IT of 3 ms and a normalized AGC target of 500%. Peptides from chemoproteomic pull-down samples were analyzed in a data-dependent acquisition (DDA) mode. The full MS spectra were analysed with Orbitrap analyser every second at the resolution of 240 000, while MS/MS spectra were acquired on Astral analyser with maximum injection time of 5 ms.

Global proteomics: data analysis

Raw files were analyzed in DIA-NN 2.2.0 [38] using an in silico DIA-NN-predicted spectral library generated from the human reference proteome (UniProtKB, 20,659 sequences, downloaded January 2026). Library generation and searching used the following settings: protease, Trypsin/P; up to 1 missed cleavage; maximum 2 variable modifications; modifications, C carbamidomethylation, N-terminal M excision, M oxidation, and protein N-terminal acetylation; peptide length 7–30; precursor charge 2–4; precursor m/z 380–980; fragment-ion m/z 150–2000; mass accuracy 10 ppm; MS1 accuracy 4 ppm; scan window 7; scoring, peptidoforms; proteotypicity, genes; machine learning, cross-validated neural networks; quantification, QuantUMS (high precision); cross-run normalization, RT-dependent; library generation, IDs, RT & IM profiling; and optimal speed/RAM usage. Match-between-runs and protein inference were enabled. The resulting pg_matrix was filtered to protein groups satisfying a Global.PG.Q.Value threshold of 0.01 using RStudio (v2024.12.1+563), and non-human cRAP proteins were excluded. The data matrix was further processed in Perseus (v2.1.5.0; [39]): intensities were log2-transformed and filtered for proteins with at least three valid values in at least one group and identified by at least two peptides. Differences between groups were assessed by paired Student's t-test (requiring at least three valid values per compared group); proteins meeting $p < 0.05$ and $|\text{fold change}| > 1.2$ were considered differential.

Chemoproteomic pull-down: data analysis

The acquired data were processed with MaxQuant software (version 2.8.0.0) [39]and searched by an integrated Andromeda search engine [40] against the human reference proteome (UniProtKB, 20,659 sequences, downloaded January 2026). The false discovery rate (FDR) for the peptide and protein identification was set to 1%. Label free quantification (LFQ) was carried out. The resulting MaxQuant output table containing protein group identifications and quantitative information (LFQ intensities) was uploaded to the Perseus platform (version 2.1.5.0) for further analysis. At the first step, the list of identified protein groups was shortened by removing proteins identified in the decoy database, contaminants and proteins only identified by site. Then, the LFQ intensities were log2-transformed. Before statistical analysis, data matrix was filtered for proteins with 100% of valid values in at least one group and for proteins identified based on at least 2 peptides. Subsequently, missing values in the filtered matrix were imputed by low constant value. To reveal changes between the experimental groups, Student's t-test followed by Benjamini-Hochberg FDR correction set to 5% was applied.

Animals and ethics

Female C57BL/6 mice (5 weeks old, 16–18 g) were housed under specific-pathogen-free (SPF) conditions at 22–25 °C and 50–60% relative humidity on a 12 h light/dark cycle, with one week of acclimatization before the start of experiments. All procedures were approved by the Institutional Animal Care and Use Committee

(IACUC) of Zhejiang University of Technology (approval no. MGS20231227191) and were performed in accordance with the Guide for the Care and Use of Laboratory Animals.

Tumor model and treatment

Human PD-L1–expressing MC38 colon carcinoma cells (Hu-PD-L1-MC38) were cultured in DMEM supplemented with 10% fetal bovine serum (Sigma) and hygromycin B (50 μg/mL) until the logarithmic growth phase (viability ≥ 95%). Cells were harvested, washed, and resuspended in cold PBS at 5×10^6 cells/mL. The right axillary region was depilated, and each mouse was inoculated subcutaneously with 5×10^5 cells in 100 μL.

When tumors reached approximately 50 mm^3 (≈ day 6), mice were randomized into four groups (n = 5): vehicle control (1% DMSO in PBS), durvalumab (2.5 mg/kg), apigenin (100 mg/kg), and combination (durvalumab + apigenin). Durvalumab was dissolved in physiological saline and administered by tail-vein injection twice weekly. Apigenin was formulated in 90% PEG300 / 10% saline and administered daily by oral gavage (250 μL). The combination group received durvalumab twice weekly and apigenin daily as described above; the vehicle group received an equal volume of 1% DMSO in PBS. Tumor volume and body weight were recorded every two days, and growth curves were plotted. Treatment was continued for 15 days, and mice were euthanized on day 16.

Sample collection and serum biochemistry

Prior to euthanasia, 200–300 μL of whole blood was collected from the orbital sinus into sodium-heparin tubes and centrifuged at 4 °C. Plasma was analyzed on an automated biochemistry analyzer for aspartate aminotransferase (AST, U/L), alanine aminotransferase (ALT, U/L), total protein (TP, g/L), albumin (ALB, g/L), urea (mmol/L), uric acid (UA, μmol/L), and creatinine (CREA, μmol/L). Tumors, hearts, livers, spleens, lungs, and kidneys were excised and weighed, and isolated tumors were photographed for morphological assessment.

NMR binding assay

^{1}H NMR measurements were carried out at room temperature on an ultra-shielded 600 MHz Jeol JNMECZ600R spectrometer equipped with the HCN Ultracool helium cryo-probe head (with z-gradient coils). To provide a lock signal, 10% (v/v) D2O was added to the samples. Water suppression was achieved with the WATERGATE sequence. The PD-L1 protein was used at a concentration of 0.2 mM. The spectra were processed with Delta 6.0 software.

Flow cytometry of peripheral blood T cells

Peripheral blood (100 μL) collected from the orbital sinus was diluted 1:1 with PBS and layered onto Ficoll-Paque PLUS. Mononuclear cells were isolated by density-

gradient centrifugation (400 ×g, 20 °C, 30 min, with low acceleration and deceleration). The buffy coat was collected, washed in three volumes of PBS (400 ×g, 20 °C, 15 min), resuspended in flow cytometry buffer, and adjusted to 1×10^6 cells/100 μL. For T-cell subset analysis, cells were stained with anti-mouse CD3, CD4, and CD8a antibodies (1 μL each) for 30 min at 4 °C in the dark, washed twice in flow cytometry buffer (1000 rpm, 4 °C, 5 min), resuspended in 200 μL of buffer, and acquired on a flow cytometer. For activation analysis, a separate aliquot was stained with anti-mouse CD3 (1 μL) and anti-mouse CD69 (1.5 μL) under identical conditions.

Isolation and flow cytometry of tumor-infiltrating lymphocytes

Tumors were excised, washed in PBS, and minced (~100 mg) into small fragments. Tissue was digested in collagenase IV (2 mg/mL; 1 mL per 100 mg tissue) in a 37 °C water bath for 1.5–2 h until visibly turbid. Digestion was stopped with complete medium, and the suspension was filtered through a 70-μm cell strainer (200 mesh). Cells were washed twice in PBS, counted, and adjusted to 5×10^5 cells/mL. For T-cell analysis, cells were stained with anti-mouse CD3, CD4, and CD8 antibodies (1 μL each) for 30 min at 4 °C in the dark, washed, resuspended in 200 μL of flow cytometry buffer, and acquired on a flow cytometer.

Immunohistochemistry

Tumors were fixed in 4% paraformaldehyde for 24 h, dehydrated, paraffin-embedded, and sectioned. After deparaffinization, sections were incubated with anti–granzyme B or anti-perforin primary antibody overnight at 4 °C, washed three times in PBS, and incubated with the corresponding secondary antibody. Staining was developed with DAB substrate; sections were then dehydrated through graded alcohols, cleared in xylene, and mounted. Images were acquired by light microscopy.

Hematoxylin and eosin (H&E) staining

Heart, liver, spleen, lung, and kidney tissues were fixed in 4% paraformaldehyde for 24 h, embedded, sectioned, dehydrated, and stained with hematoxylin and eosin. Sections were mounted in neutral resin and imaged by microscopy.

Data availability

All data generated during this study are included in this published article and its supplementary files.

The mass spectrometry data from chemoproteomic pull-down experiment were deposited to the ProteomeXchange Consortium (Vizcaíno et al., 2014) via the MassIVE repository with the dataset identifier PXD081543 (MassIVE identifier: MSV000102578). The mass spectrometry data from global proteome analysis were deposited to the ProteomeXchange Consortium (Vizcaíno et al., 2014) via the MassIVE repository with the dataset identifier PXD081544 (MassIVE identifier: MSV000102579). The deposited dataset from global proteome analysis contains raw files from more extended experiment, including control group, apigenin treatment and

combined apigenin plus durvalumab treatment; in this article the comparison between combined apigenin plus durvalumab treatment (API+DUR) and control group (CON) was presented.

Abbreviations

LAG-3, lymphocyte-activation gene 3; PD-1, programmed cell death protein 1; PD-L1, programmed death-ligand 1; MHCII, major histocompatibility complex class II; FGL1, fibrinogen-like protein 1; ICB, immune checkpoint blockade; HTRF, homogeneous time-resolved fluorescence; FRET, Förster resonance energy transfer; IC50, half-maximal inhibitory concentration; EC50, half-maximal effective concentration; MST, microscale thermophoresis; TRIC, temperature-related intensity change; Kd, dissociation constant; NMR, nuclear magnetic resonance; SAR, structure–activity relationship; PBMC, peripheral blood mononuclear cells; APC, antigen-presenting cell; TIL, tumor-infiltrating lymphocyte; MFI, mean fluorescence intensity; IFN-γ, interferon gamma; TNF-α, tumor necrosis factor alpha; IL-2, interleukin-2; PMA, phorbol 12-myristate 13-acetate; TGI, tumor growth inhibition; IHC, immunohistochemistry; H&E, hematoxylin and eosin; DIA, data-independent acquisition; LC-MS/MS, liquid chromatography–tandem mass spectrometry; GO, Gene Ontology; DMSO, dimethyl sulfoxide; PEG, polyethylene glycol; IACUC, Institutional Animal Care and Use Committee.

Acknowledgements

Declaration of generative AI use in the writing process

During the preparation of this work, the authors used a generative artificial-intelligence assistant (Claude, Anthropic) to polish the language and grammar of the final text. The authors reviewed and edited all AI-assisted content and take full responsibility for the content of the published article.

Funding

This research has been supported (to J.P.) by the Opus Grant No. UMO-2024/53/B/NZ7/02801 from the National Science Centre, Poland. The animal experimental work was supported by the National Natural Science Foundation of China (NSFC, grant number 22177105). The study was carried out using the research infrastructure cofunded by the European Union in the framework of the Smart Growth Operational Program, Measure 4.2; Grant No. POIR.04.02.00-00-D001/20, “ATOMIN 2.0–ATOMic scale science for the INnovative economy. The purchase of Orbitrap Astral Mass Spectrometer has been supported by a grant from the Priority Research Area (POB BioS) under the Strategic Programme Excellence Initiative at Jagiellonian University.

Contributions

Conceptualization, W.Z. and J.P.; Study design&Methodology, W.Z., J.P., K.B., M.L., P.L., S.W., K.N., J.K.-K., J.C.-P., A.S.-K., R.F., J.K.-T., M.K., S.B., K.M.-M., E.S., B.M., B.S.-R., U.J., W.Z. and J.P.; Investigation, K.B., M.L., P.L., S.W., K.N., J.K.-K., J.C.-P., A.S.-K., R.F., J.K.-T., M.K., S.B., K.M.-M., E.S., B.M., B.S.-R. and U.J.; Protein expression and purification, K.B. and K.M.-M.; HTRF binding assays, K.B.; E.S.; Microscale thermophoresis, K.B.; NMR-based binding experiments, B.M.; Molecular docking and modeling, R.F., J.K.-T. and M.K.; Photoaffinity pull-down and proteomics, S.W., S.B., B.S.-R. and U.J.; Cell-based reporter and viability assays, K.N.; S.W.; J.K.-K.; PBMC isolation, culture, and flow cytometry, M.L. and K.N.; In vivo tumor studies in mice, P.L. and W.Z.; Immunohistochemistry and histopathology, P.L. and W.Z.; Formal analysis and statistics, K.B. and J.P.; Data visualization, K.B. and J.P.; M.L.; Apigenin formulation and solid-state characterization, J.C.-P. and A.S.-K.; Writing – original draft, K.B. and J.P.; Writing – review and editing, K.B., M.L., P.L., S.W., K.N., J.K.-K., J.C.-P., A.S.-K., R.F., A.D., J.K.-T., M.K., S.B., K.M.-M., E.S., B.M., M.S., B.S.-R., U.J., W.Z. and J.P.; Funding acquisition, J.P. and W.Z.; Supervision, J.P., W.Z., A.D., J.K.-T., J.C.-P. and M.S. J.P. was the principal investigator responsible for the protein-based work and for the supervision and major editing of the final manuscript; W.Z. was the principal investigator responsible for the in vivo mouse experiments. All authors have read and agreed to the final version of the manuscript.

The authors thank Łukasz Skalniak for overseeing the wet-laboratory work of Justyna Kocik-Król and Katarzyna Nakielska.

Corresponding author

Correspondence to Jacek Plewka and Wen Zhang

References

1. Ribas A, Wolchok JD. Cancer immunotherapy using checkpoint blockade. Science. American Association for the Advancement of Science; 2018;359:1350–5. https://doi.org/10.1126/science.aar4060

2. Tumeh PC, Harview CL, Yearley JH, Shintaku IP, Taylor EJM, Robert L, et al. PD-1 blockade induces responses by inhibiting adaptive immune resistance. Nature. Nature Publishing Group; 2014;515:568–71. https://doi.org/10.1038/nature13954

3. Triebel F, Jitsukawa S, Baixeras E, Roman-Roman S, Genevee C, Viegas-Pequignot E, et al. LAG-3, a novel lymphocyte activation gene closely related to CD4. J Exp Med. 1990;171:1393–405. https://doi.org/10.1084/jem.171.5.1393

4. Tawbi HA, Schadendorf D, Lipson EJ, Ascierto PA, Matamala L, Gutiérrez EC, et al. Relatlimab and Nivolumab versus Nivolumab in Untreated Advanced Melanoma. New England Journal of Medicine. Massachusetts Medical Society; 2022;386:24–34. https://doi.org/10.1056/NEJMoa2109970

5. Huard B, Mastrangeli R, Prigent P, Bruniquel D, Donini S, El-Tayar N, et al. Characterization of the major histocompatibility complex class II binding site on LAG-

3 protein. Proceedings of the National Academy of Sciences. Proceedings of the National Academy of Sciences; 1997;94:5744–9. https://doi.org/10.1073/pnas.94.11.5744

6. Maruhashi T, Sugiura D, Okazaki I, Shimizu K, Maeda TK, Ikubo J, et al. Binding of LAG-3 to stable peptide-MHC class II limits T cell function and suppresses autoimmunity and anti-cancer immunity. Immunity. 2022;55:912-924.e8. https://doi.org/10.1016/j.immuni.2022.03.013

7. Wang J, Sanmamed MF, Datar I, Su TT, Ji L, Sun J, et al. Fibrinogen-like Protein 1 Is a Major Immune Inhibitory Ligand of LAG-3. Cell. 2019;176:334-347.e12. https://doi.org/10.1016/j.cell.2018.11.010

8. Yoshida T, Nakamoto T, Atsumi N, Ohe C, Sano T, Yasukochi Y, et al. Impact of LAG-3/FGL1 pathway on immune evasive contexture and clinical outcomes in advanced urothelial carcinoma. J Immunother Cancer . BMJ Publishing Group Ltd; 2024 [cited 2026 Aug 15];12. https://doi.org/10.1136/jitc-2024-009358

9. Chihara N, Madi A, Kondo T, Zhang H, Acharya N, Singer M, et al. Induction and transcriptional regulation of the co-inhibitory gene module in T cells. Nature. Nature Publishing Group; 2018;558:454–9. https://doi.org/10.1038/s41586-018-0206-z

10. Xiang S, Li S, Xu J. Unravelling T cell exhaustion through co-inhibitory receptors and its transformative role in cancer immunotherapy. Clinical and Translational Medicine. 2025;15:e70345. https://doi.org/10.1002/ctm2.70345

11. Yokosuka T, Takamatsu M, Kobayashi-Imanishi W, Hashimoto-Tane A, Azuma M, Saito T. Programmed cell death 1 forms negative costimulatory microclusters that directly inhibit T cell receptor signaling by recruiting phosphatase SHP2. J Exp Med. 2012;209:1201–17. https://doi.org/10.1084/jem.20112741

12. Konstantinidou M, Zarganes-Tzitzikas T, Magiera-Mularz K, Holak TA, Dömling A. Immune Checkpoint PD-1/PD-L1: Is There Life Beyond Antibodies? Angewandte Chemie International Edition. 2018;57:4840–8. https://doi.org/10.1002/anie.201710407

13. Yang J, Hu L. Immunomodulators targeting the PD-1/PD-L1 protein-protein interaction: From antibodies to small molecules. Medicinal Research Reviews. 2019;39:265–301. https://doi.org/10.1002/med.21530

14. Dong S, Guo X, Han F, He Z, Wang Y. Emerging role of natural products in cancer immunotherapy. Acta Pharmaceutica Sinica B. 2022;12:1163–85. https://doi.org/10.1016/j.apsb.2021.08.020

15. Yan C, Wang G. Advances in research on flavonoids in tumor immunotherapy (Review). Molecular Medicine Reports. Spandidos Publications; 2025;31:1–16. https://doi.org/10.3892/mmr.2025.13515

16. Madunić J, Madunić IV, Gajski G, Popić J, Garaj-Vrhovac V. Apigenin: A dietary flavonoid with diverse anticancer properties. Cancer Letters. 2018;413:11–22. https://doi.org/10.1016/j.canlet.2017.10.041

17. Coombs MRP, Harrison ME, Hoskin DW. Apigenin inhibits the inducible expression of programmed death ligand 1 by human and mouse mammary carcinoma cells. Cancer Letters. 2016;380:424–33. https://doi.org/10.1016/j.canlet.2016.06.023

18. Xu L, Zhang Y, Tian K, Chen X, Zhang R, Mu X, et al. Apigenin suppresses PD-L1 expression in melanoma and host dendritic cells to elicit synergistic therapeutic effects. J Exp Clin Cancer Res. 2018;37:261. https://doi.org/10.1186/s13046-018-0929-6

19. Zhang J, Huang Y, Liu D, Gao Y, Qian S. Preparation of apigenin nanocrystals using supercritical antisolvent process for dissolution and bioavailability enhancement. European Journal of Pharmaceutical Sciences. 2013;48:740–7. https://doi.org/10.1016/j.ejps.2012.12.026

20. Huang S, Xue Q, Xu J, Ruan S, Cai T. Simultaneously Improving the Physicochemical Properties, Dissolution Performance, and Bioavailability of Apigenin and Daidzein by Co-Crystallization With Theophylline. Journal of Pharmaceutical Sciences. 2019;108:2982–93. https://doi.org/10.1016/j.xphs.2019.04.017

21. Bhujbal SV, Mitra B, Jain U, Gong Y, Agrawal A, Karki S, et al. Pharmaceutical amorphous solid dispersion: A review of manufacturing strategies. Acta Pharmaceutica Sinica B. 2021;11:2505–36. https://doi.org/10.1016/j.apsb.2021.05.014

22. Rana JN, Gul K, Mumtaz S. Isorhamnetin: Reviewing Recent Developments in Anticancer Mechanisms and Nanoformulation-Driven Delivery. International Journal of Molecular Sciences. Multidisciplinary Digital Publishing Institute; 2025;26:7381. https://doi.org/10.3390/ijms26157381

23. Liu K, Zhao F, Yan J, Xia Z, Jiang D, Ma P. Hispidulin: A promising flavonoid with diverse anti-cancer properties. Life Sciences. 2020;259:118395. https://doi.org/10.1016/j.lfs.2020.118395

24. de Morais EF, de Oliveira LQR, Farias Morais HG de, Souto Medeiros MR de, Freitas R de A, Rodini CO, et al. The Anticancer Potential of Kaempferol: A Systematic Review Based on In Vitro Studies. Cancers. Multidisciplinary Digital Publishing Institute; 2024;16:585. https://doi.org/10.3390/cancers16030585

25. Wang J, Li H, Wang Z, Ruan S. Luteolin: A Comprehensive and Visualized Analysis of Research Hotspots and Its Antitumor Mechanisms. Am J Chin Med. World Scientific Publishing Co.; 2024;52:2377–401. https://doi.org/10.1142/S0192415X24500903

26. Konieczny M, Musielak B, Kocik J, Skalniak L, Sala D, Czub M, et al. Di-bromo-Based Small-Molecule Inhibitors of the PD-1/PD-L1 Immune Checkpoint. J Med Chem. 2020;63:11271–85. https://doi.org/10.1021/acs.jmedchem.0c01260

27. Slota A, Golebiowska-Mendroch K, Kocik-Krol J, Musielak B, Stec M, Weglarczyk K, et al. Characterization of Clinically Evaluated Small-Molecule Inhibitors of PD-L1 for Immunotherapy. ACS Med Chem Lett. 2025;16:1359–64. https://doi.org/10.1021/acsmedchemlett.5c00245

28. Zhang H, Zhou S, Plewka J, Wu C, Zhu M, Yu Q, et al. Design, Synthesis, and Antitumor Activity Evaluation of 2-Arylmethoxy-4-(2,2′-dihalogen-substituted biphenyl-3-ylmethoxy) Benzylamine Derivatives as Potent PD-1/PD-L1 Inhibitors. J Med Chem. 2023;66:10579–603. https://doi.org/10.1021/acs.jmedchem.3c00731

29. Zhang F, Zhang H, Zhou S, Plewka J, Wang M, Sun S, et al. Design, synthesis, and evaluation of antitumor activity of 2-arylmethoxy-4-(2-fluoromethyl-biphenyl-3-ylmethoxy) benzylamine derivatives as PD-1/PD-l1 inhibitors. European Journal of Medicinal Chemistry. 2024;276:116683. https://doi.org/10.1016/j.ejmech.2024.116683

30. Silberstein JL, Du J, Chan K-W, Frank JA, Mathews II, Kim YB, et al. Structural insights reveal interplay between LAG-3 homodimerization, ligand binding, and function. Proceedings of the National Academy of Sciences. Proceedings of the National Academy of Sciences; 2024;121:e2310866121. https://doi.org/10.1073/pnas.2310866121

31. Stasiłowicz-Krzemień A, Rosiak N, Racaniello GF, Denora N, Cielecka-Piontek J. Effective and Stable Senomorphic Apigenin Delivery System Obtained by Supercritical Carbon Dioxide Processing. International Journal of Molecular Sciences. Multidisciplinary Digital Publishing Institute; 2025;26:8126. https://doi.org/10.3390/ijms26178126

32. Salehi B, Venditti A, Sharifi-Rad M, Kręgiel D, Sharifi-Rad J, Durazzo A, et al. The Therapeutic Potential of Apigenin. International Journal of Molecular Sciences. Multidisciplinary Digital Publishing Institute; 2019;20:1305. https://doi.org/10.3390/ijms20061305

33. Verdonk ML, Cole JC, Hartshorn MJ, Murray CW, Taylor RD. Improved protein-ligand docking using GOLD. Proteins. 2003;52:609–23. https://doi.org/10.1002/prot.10465

34. Korb O, Stützle T, Exner TE. Empirical scoring functions for advanced protein-ligand docking with PLANTS. J Chem Inf Model. 2009;49:84–96. https://doi.org/10.1021/ci800298z

35. Abraham MJ, Murtola T, Schulz R, Páll S, Smith JC, Hess B, et al. GROMACS: High performance molecular simulations through multi-level parallelism from laptops to supercomputers. SoftwareX. 2015;1–2:19–25. https://doi.org/10.1016/j.softx.2015.06.001

36. Vanommeslaeghe K, Hatcher E, Acharya C, Kundu S, Zhong S, Shim J, et al. CHARMM general force field: A force field for drug-like molecules compatible with the CHARMM all-atom additive biological force fields. J Comput Chem. 2010;31:671–90. https://doi.org/10.1002/jcc.21367

37. Mark P, Nilsson L. Structure and Dynamics of the TIP3P, SPC, and SPC/E Water Models at 298 K. J Phys Chem A. 2001;105:9954–60. https://doi.org/10.1021/jp003020w

38. Demichev V, Messner CB, Vernardis SI, Lilley KS, Ralser M. DIA-NN: neural networks and interference correction enable deep proteome coverage in high throughput. Nat Methods. 2020;17:41–4. https://doi.org/10.1038/s41592-019-0638-x

39. Tyanova S, Temu T, Cox J. The MaxQuant computational platform for mass spectrometry-based shotgun proteomics. Nat Protoc. Nature Publishing Group; 2016;11:2301–19. https://doi.org/10.1038/nprot.2016.136

40. Cox J, Neuhauser N, Michalski A, Scheltema RA, Olsen JV, Mann M. Andromeda: a peptide search engine integrated into the MaxQuant environment. J Proteome Res. 2011;10:1794–805. https://doi.org/10.1021/pr101065j

Supplementary Files

This is a list of supplementary files associated with this preprint. Click to download.

- apigeninsupplementaryfigures.pdf